Estonian Journal of Earth Sciences
2026, **75**, 2, 103–121

https://doi.org/10.3176/earth.2026.07

www.eap.ee/earthsciences
Estonian Academy Publishers

RESEARCH ARTICLE

Received 12 January 2026
Accepted 14 July 2026
Available online 23 October 2026

Keywords:
UAV-SfM photogrammetry, coastal geomorphology, Baltic Klint

Corresponding author:
Tiia-Linda Purge
tiia-linda.purge@ut.ee

Citation:
Purge, T.-L., Kohv, M., Liira, M. and Harak, T. 2026. Using 3D modelling to identify cliff erosion processes and their controls and to map and predict geohazards: a case study of Pakri Cliff, Estonia. *Estonian Journal of Earth Sciences*, **75**(2), 103–121. https://doi.org/10.3176/earth.2026.07

© 2026 Authors. This is an open access article distributed under the terms and conditions of the Creative Commons Attribution (CC BY) license (http://creativecommons.org/licenses/by/4.0).

Using 3D modelling to identify cliff erosion processes and their controls and to map and predict geohazards: a case study of Pakri Cliff, Estonia

Tiia-Linda Purge[a], Marko Kohv[a], Martin Liira[a,b] and Tiina Harak[a]

[a] Department of Geology, University of Tartu, Ravila 14a, 50411 Tartu, Estonia

[b] Department of Marine Geology, Geological Survey of Estonia, F. R. Kreutzwaldi 5, 44314 Rakvere, Estonia

ABSTRACT

Coastal zones, particularly those with low-lying areas, are increasingly affected by anthropogenic pressures and climate change. Rocky and cliffed coasts, slow-evolving geomorphic systems, experience erosional processes that pose significant geohazards. Understanding the controls on cliff retreat is critical for predicting coastal evolution, assessing geological risk, and supporting land-use and heritage management. This study integrates 2D orthophoto interpretation with high-resolution 3D unmanned aerial vehicle-based structure-from-motion (UAV-SfM) photogrammetry to link structural geological mapping with quantitative change detection, thereby improving the precision and spatial coverage of cliff-change analysis. Three 3D models of Pakri Cliff, derived from datasets collected in 2015, 2022, and 2024, were used to quantify cliff retreat and characterise key geological features, including strata, joint systems, and coastal notches. Results indicate a mean retreat rate of 18 cm/year. While erosion rates vary with lithology, their relative distribution remains stable over time, maintaining a distinct vertical profile. Coastal notches are initiated along joints and progressively modified by marine dynamics. These findings highlight that cliff erosion at Pakri is a multi-mechanism process controlled by geological structure, weathering, mass movement, and wave action, all of which exhibit high spatiotemporal variability. Ultimately, this integrated approach demonstrates how coupling structural geology with high-resolution monitoring enhances the detection of geohazards and provides a more comprehensive understanding of long-term cliff evolution mechanisms.

1. Introduction

Global climate change and an increasing atmospheric energy budget (Calvin et al. 2023) are driving widespread transformations in natural systems, reshaping ecosystems (Grimm et al. 2013) and altering the characteristics of extreme weather events (Walsh et al. 2020). Low-lying coastal areas are particularly threatened by sea-level rise, storm surges, and wind stress, which drive flooding and accelerate coastal processes (Nicholls and Cazenave 2010; Pryor et al. 2012).

According to Weisse et al. (2021), in the Baltic Sea, long-term changes in relative mean sea level are affected by postglacial rebound, freshwater input, wind stress, and regional specificities such as thermosteric and halosteric contributions. Storms are most frequent in autumn and winter (Jaagus and Suursaar 2013; Wolski and Wiśniewski 2021), bringing high waves that control nearshore sediment transport, beach profiles, and morphology (Miller 1999). As noted by Soomere et al. (2013), significant spatial variability in wave heights and closure depths along the eastern Baltic coast leads to heterogeneous impacts on coastal processes. While ripple-induced sediment transport can slow local erosion (Tõnisson et al. 2011), small shifts in wind direction can profoundly alter coastal erosion patterns, increasing the vulnerability of previously protected areas (Soomere 2024). A gradual decline in sea ice occurrence and earlier breakup further alters wave properties and nearshore sediment transport (Sooäär and Jaagus 2007; Manson 2022). Although average wave characteristics change little under partial ice cover (Najafzadeh and Soomere 2024), the complete loss of sea ice may substantially increase cumulative wave energy. According to Dodge et al. (2022), sea ice can both act as a protective barrier against storms and serve as an erosive agent.

Despite both anthropogenic and natural pressures, coastal zones possess high environmental, economic, and social value. Beaches and seashores provide important recreational functions, harbour infrastructure supports transport and trade, and residential development values proximity to the coast and sea views. Consequently, effective monitoring of short- and long-term coastal processes across a range of coastal typologies is essential for risk assessment and management. Traditional monitoring approaches, such as repeated real-time kinematic global navigation satellite system (RTK-GNSS) surveys, often lack spatial and temporal resolution, and complementing these approaches with modern techniques enhances accuracy, efficiency, and long-term comparability.

Emerging remote sensing methods offer cost-effective alternatives. Unmanned aerial vehicle (UAV)-based structure-from-motion (SfM) photogrammetry enables rapid acquisition of high-resolution data, 3D modelling, and detailed analysis of coastal morphology (James and Robson 2012; Wang et al. 2019; Adade et al. 2021; Cirillo et al. 2024). The rapid development of UAV technology and expansion of the commercial market have led to improvements in many aspects, including sensors, navigation systems, and software (Klemas 2015). Therefore, drones and mounted sensors have widespread applications across the geosciences (James and Robson 2012; Westoby et al. 2012). UAVs provide numerous advantages over traditional monitoring methods, such as near real-time data collection, customisable temporal and spatial coverage, lower operational costs, greater flexibility, and access to otherwise hard-to-reach areas, although challenges such as weather dependency, sensor limitations, flight safety regulations, and pilot training remain (Berra and Peppa 2020).

This approach addresses the limitations of widespread 2D mapping, which relies primarily on the position of the cliff edge, thereby ignoring structural changes occurring along the mid-cliff or at the base (Letortu et al. 2025). Where a cliff displays contrasting lithologies or variable retreat rates in its vertical section, monitoring changes beneath the cliff edge is critical for detecting erosional asymmetry (Young et al. 2009; Menier et al. 2025) and potential locations of cliff failure (Swirad and Young 2025). Drones and mounted sensors thus hold considerable potential that has not yet been fully exploited in Estonian coastal science. This study aims to enhance the precision and spatial coverage of cliff-change analysis by integrating 2D orthophoto interpretation with 3D UAV-SfM mapping, thereby linking structural geological mapping with quantitative change detection to provide a more comprehensive understanding of Pakri Cliff retreat.

2. Study site

The Pakri Peninsula and Pakri Cliff, part of the Baltic Klint, are located in northwestern Estonia between Lahepera and Pakri Bays (Fig. 1). The cornice-shaped escarpment reaches a height of up to 25 m above sea level, gradually decreasing in elevation towards the southeast. The area's land uplift rate relative to the geoid is around 3 mm/year (Suursaar and Kall 2018; Vestøl et al. 2019). Over the past decade, however, the accelerating global sea-level rise (~3.7 mm/year; Calvin et al. 2023) has outpaced this uplift rate, resulting in a positive relative sea-level trend at Pakri at present.

The cliff profile exposes a composite section of Ordovician and Cambrian sediments with varying lithologies (Fig. 2). The upper third (~7 m) consists of Middle Ordovician car-

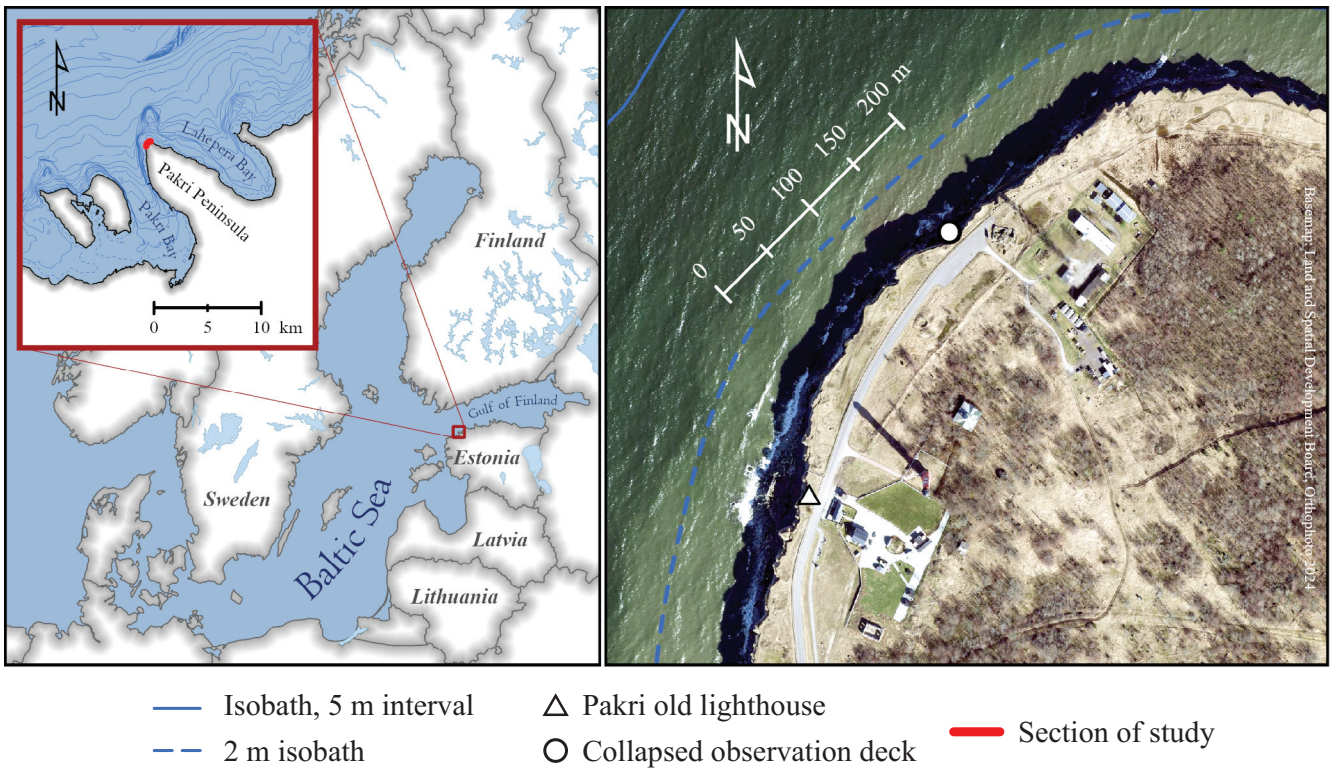


Fig. 1. Geographical location of Pakri Cliff. Basemap orthophoto (2024) and depth isobaths from the Republic of Estonia Land and Spatial Development Board.

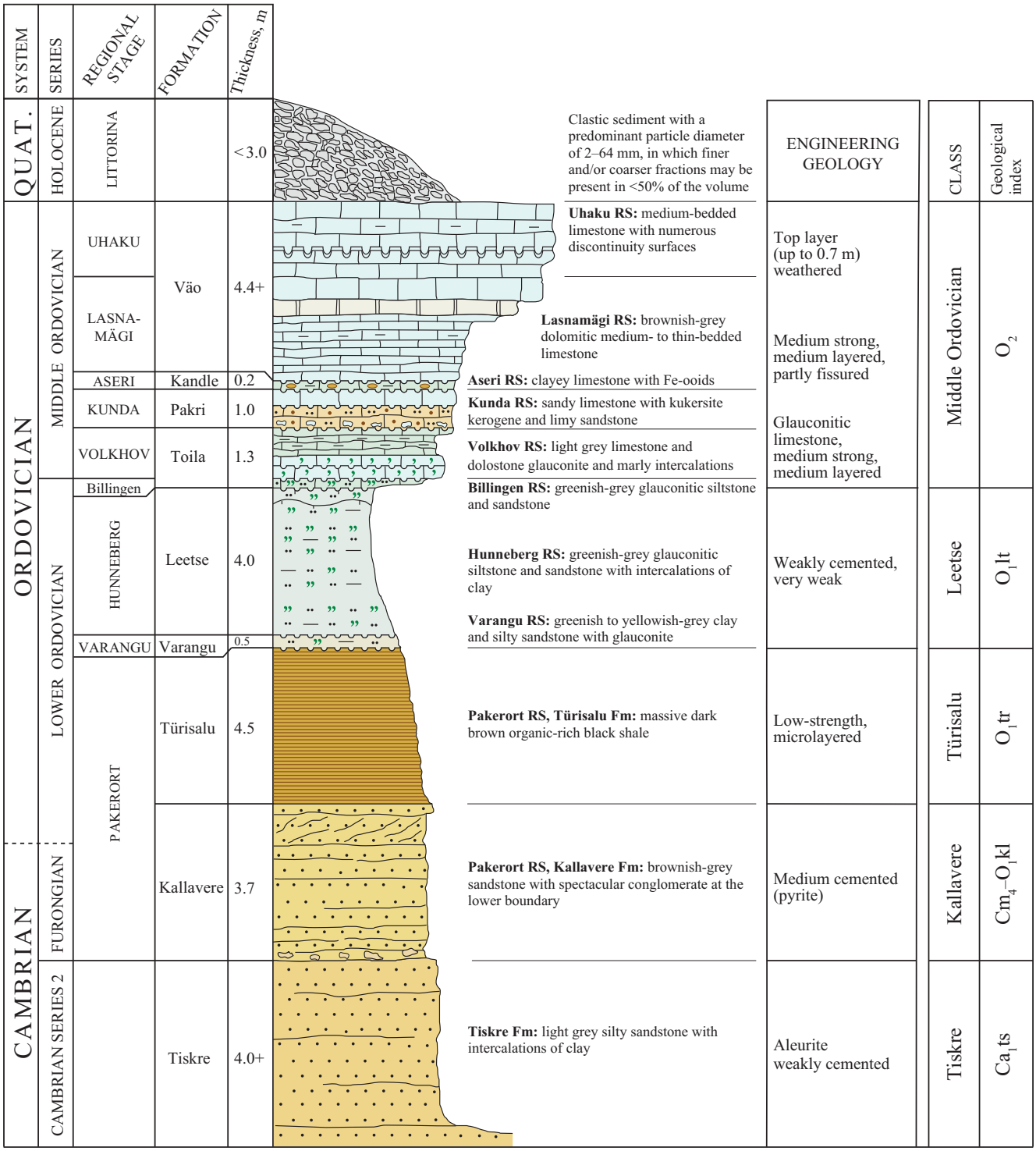


Fig. 2. Composite section of the Pakri Peninsula. Modified by Hints et al. (2024) after Mens and Puura (1996). The cross-section has been complemented with a description of the top layer, engineering geological data from the Estonian Geological Archive, and the classification used in the study. Abbreviations: QUAT. – Quaternary, RS – regional stage, Fm – formation.

bonates, mainly medium- to thin-bedded pack- and wackestones. This section is strongly jointed due to tectonic stresses, producing a characteristic zigzag cliff edge. According to Miidel and Raukas (2005), the mean distance of NW–SE joints is 0.5–3 m (seldom up to 10 m), while that of joints with a NE–SW orientation is 2–3.5 m (seldom 25–40 m). Orthogonal joint systems are least frequent, with distances between them ranging from 8 to 40 m. Beneath the carbonates lie Lower Ordovician, Furongian, and Lower Cambrian sand- and siltstones interbedded with clay. Vertically lower formations (Fms), such as Kallavere and Tiskre, are subject to wave abrasion, and coastal notches have formed. The carbonates undergo rapid rockfall due to transversely oriented diaglacial joints and the regression of the underlying rock. Fallen limestone blocks form a talus that protects the cliff base from erosion until the talus is also eroded.

2.1. Climatic overview

The Pakri Peninsula has a transitional climate (Fig. 3). The mean annual temperature is 7.0 °C, ranging from –2.6 °C in February to 17.6 °C in July. Total annual precipitation is approximately 580 mm, with the majority – approximately

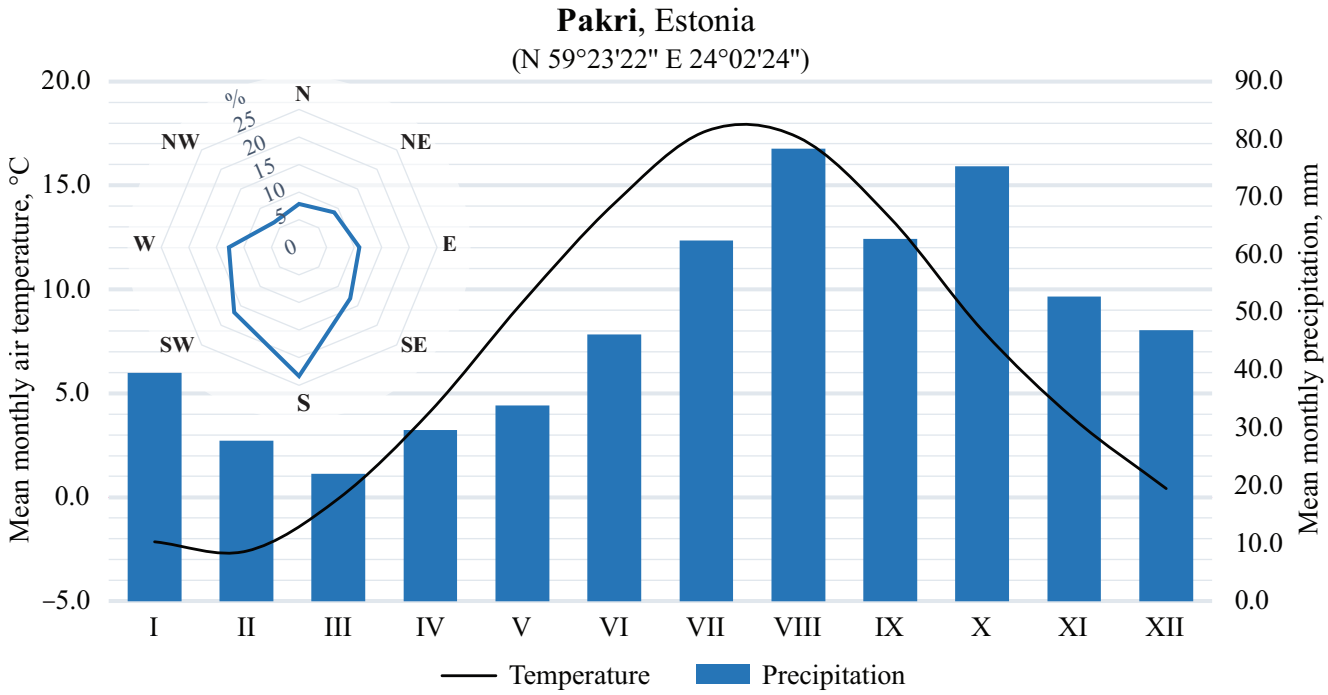


Fig. 3. Pakri climate diagram and wind rose based on measurements from the Pakri meteorological station. The figures are derived from hourly data collected over the past 20 years (January 2004 to December 2023). Precipitation measurements from November to March may differ from actual values, as the early data (2004–2009) were recorded using a device that was not operational during the winter season.

60% – falling between July and November. The prevailing winds are typically stronger and originate from the south, southwest, and west. The annual average wind speed is 4.6 m/s, with higher velocities observed during late autumn and early winter and lower velocities from May to August.

Wave climate in the Baltic Sea can differ from region to region due to the variety of wind fields and complex geometry. Soomere and Räämet (2011) consolidated temporal variations and spatial patterns in the wave properties of the Gulf of Finland, using Pakri as a long-term coastal observation site, which is primarily exposed to waves generated in the northern Baltic Proper (Zaitseva-Pärnaste et al. 2009). Drawing on previously mentioned studies, the dominant wave approach direction is from the west, with interannual and interdecadal variability. The distribution of wave intensities is considered relatively consistent. The wave regime is generally mild, with a long-term mean wave height of approximately 0.6–0.65 m. The local wave climate also exhibits clear seasonal patterns in wave height, with maximum values from October to January and minimum values from March to August, and a clear minimum in April or May.

2.2. Previous studies

The terrestrial part of the Baltic Klint formation represents a key geotourism destination and has been the focus of geological research for over two centuries (Tuuling et al. 2011), primarily concerning its geological composition. Orviku et al. (2013) studied the retreat rates of cliffs and scarps with different geological properties, using aerial photographs, topographic maps, and the distance of the cliff edge from a remarkable landmark. Their analyses revealed that over a 275-year period, the cliff had retreated by approximately 70 m, i.e. 25 cm/year. However, excluding the impact of the major March 2008 collapse, the rate would be approximately 20 cm/year. According to Miidel and Raukas (2005) and Orviku et al. (2013), the long-term retreat results from the interplay between wave erosion and weathering. While Miidel and Raukas (2005) focus on geological preconditions – such as horizontal bedding and joint systems – and mechanical triggers – such as freeze–thaw cycles and groundwater fluctuations – that initiate mass movements, Orviku et al. (2013) emphasise that hydrodynamic factors are the primary drivers that sustain erosion by removing protective talus from the cliff foot.

3. Materials and methods

Our primary method for monitoring cliff dynamics was UAV-based photogrammetry, a technique that derives accurate measurements from photographs without direct contact with the subject. To generate a 3D model from a series of 2D images, stereo vision techniques are employed, whereby spatial coordinates are computed by capturing the object from multiple viewpoints (Linder 2009).

According to James et al. (2019), the typical photogrammetry workflow in geomorphic research consists of survey design (image capture and photogrammetric control), survey execution, photogrammetric processing, and reporting of results, together with insight into model quality, such as errors, uncertainty, and image network performance. As noted by Turner et al. (2014), while UAV-based photogrammetry presents several advantages over traditional methods, it is still confronted with challenges such as considerable perspective distortions, variable scale, and excessive image overlap.

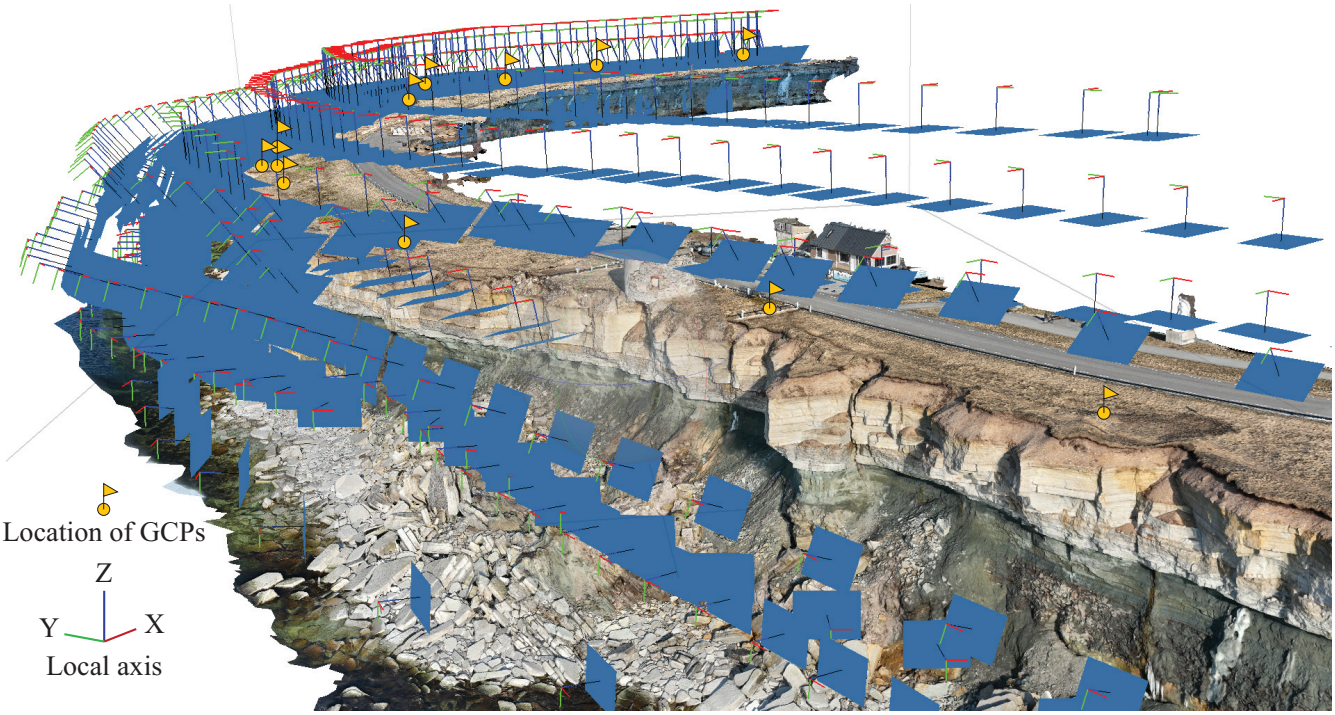


Fig. 4. Image coverage and ground control points (GCPs) in the March 2024 model.

To overcome some of these difficulties, structure-from-motion–multi-view stereo (SfM-MVS) photogrammetry has been implemented (Jiang et al. 2020).

The classical SfM-MVS pipeline consists of three main steps: scale-invariant feature transform (SIFT), SfM, and MVS. Initially, unique key points from multiple images are detected using computer vision and detection algorithms, such as SIFT. Based on the identified key points, feature matching is performed to establish correspondences across images. Based on the matched image points, a mathematical model of the camera is calculated. Bundle adjustment is an iterative optimisation process during which camera poses and parameters are simultaneously computed to minimise geometrical distortions. With optimised camera parameters, MVS algorithms are applied to perform pixel-level matching across multiple images to produce a dense point cloud. This final point cloud enables detailed 3D reconstruction, suitable for further processing steps such as mesh generation and texturing (Iglhaut et al. 2019). The quality of the photogrammetric model depends on camera parameters, surface characteristics, environmental conditions, image acquisition, and software (Barba et al. 2019; Feng et al. 2019; Deliry and Avdan 2024).

3.1. Data acquisition process

Field campaigns took place in May 2015, October 2022, and March and May 2024, preceded by survey design planning and weather observations. To achieve comprehensive coverage of the cliff face, flights were conducted across three distinct zones due to the high risk of losing the communication signal between the UAV and the operator (Fig. 4). The first zone was surveyed at an altitude of 30 m and covered the area inland of the cliff edge. In the second zone, the UAV captured images on the seaward side of the cliff edge, maintaining a low altitude of just a few metres. The third zone was surveyed to obtain images of the cliff face. For georeferencing, six black-and-white markers and six persistent natural markers used as ground control points (GCPs) were measured using the HIPER Digital UHV 2 RTK-GPS system in March 2024. The markers were placed on the cliff edge so that they evenly covered its entire length.

3.1.1. Drones and cameras

During the survey, three different drones equipped with integrated cameras were employed for image capture: the DJI Phantom 2 Vision (2015), the DJI Phantom 4 RTK SDK (2022), and the DJI Mavic 3M (2024). The general specifications and camera details for each drone and camera are provided in Table A1.

3.1.2. Photogrammetry workflow

The SfM-MVS photogrammetry workflow was performed using Agisoft Metashape Professional v2.1.3 software. First, a quality check was conducted on all images based on visual inspection and an estimated image quality feature calculated based on the sharpness level of the most focused part of the image (a Metashape feature); those deemed to be of insufficient quality were excluded. The selection of high-quality images is the basis for an accurate model. Second, images were aligned based on the same points found in several images; if the matching was successful, the key points became tie points. The resulting sparse point clouds were cleaned using the gradual selection command. We deleted 10% of the points with the highest reprojection error, then 10% with the highest reconstruction error, and finally 10% of the points with the highest projection accuracy error. During the cleaning process, attention was given to ensuring that the points did not aggregate into large clusters within the cliff area. This precaution was taken to preserve the spatial

Table 1. Overview of survey, image, camera, and model parameters. Abbreviations: RGB – red, green, and blue, X – easting, Y – northing, Z – altitude

Year	Month	Survey	RGB images		Camera parameters				
		Drone	Count	Range of estimated image quality ratings	Tie points/ projections	Ground resolution, mm/pixel	Pixel size, µm	Reprojection error, pixel	Average camera location error, cm
2015	5	DJI Phantom 2 Vision	209	0.74–0.81	57 400/ 402 120	13.2	1.41 × 1.41	1.64	X: 4.83 Y: 9.54 Z: 4.77 XY: 10.69 TOTAL: 11.71
2022	10	DJI Phantom 4 RTK SDK	711	0.77–0.85	398 302/ 1 538 988	8.67	2.41 × 2.41	1.09	X: 2.32 Y: 2.13 Z: 6.25 XY: 3.15 TOTAL: 7.00
2024	3	DJI Mavic 3M	671	0.75–0.91	362 680/ 1 842 738	8.79	3.36 × 3.36	0.59	X: 3.30 Y: 1.30 Z: 19.95 XY: 3.80 TOTAL: 20.31
2024	5	DJI Mavic 3M	1027	0.31–0.88	349 440/ 2 054 773	9.29	3.36 × 3.36	0.62	X: 15.45 Y: 32.90 Z: 64.82 XY: 36.35 TOTAL: 74.32

distribution and integrity of the data, preventing the potential loss of important details. Camera parameters and the model were updated, and a high-quality dense point cloud was calculated from depth maps. Depth maps derived from the images were also used to reconstruct the model's surface, and gaps in the point cloud were interpolated. The texture was then projected pixel by pixel directly from the original photos.

3.1.3. Georeferencing

We employed a combination of absolute and relative georeferencing approaches to ensure both absolute location within geographic space and relative alignment between the models. Absolute georeferencing relied on UAV-RTK (operational in 2022 and March 2024), utilising the closest ESTPOS GNSS reference station, as well as GCPs collected in March 2024. Each GCP marker was detected in at least three good-quality images, and the accuracy of the scaling was assessed by comparing the measured GCP coordinates with those derived directly from the model. Based on this assessment, the total root mean square error (RMSE) for the March 2024 model was 2.18 cm, while the referencing errors across all other flights ranged from 1.85 cm to 3.31 cm.

For relative georeferencing, the March 2024 model served as the reference dataset, as it had already been established with correct absolute positioning. Since there were no measured GCPs in 2015, 2022, and May 2024, persistent natural markers were used to align the models with the reference dataset. In CloudCompare, the models were referenced using point picking followed by the iterative closest point (ICP) algorithm. The transformation matrix was initially calculated using a smaller subset of the stable area and subsequently applied to the entire model. The accuracy of relative georeferencing was evaluated using the RMSE, which was 0.02 m for the 2022 and 0.03 m for the 2015 and May 2024 models.

3.2. Insight into model quality

The quality of the photogrammetric model was assessed using four metrics: image quality and overlap, confidence, reprojection, and average camera location error, as well as by visual assessment (Table 1).

Image quality and sufficient overlap are the foundation for a high-quality photogrammetric model. In general, nadir images exhibited consistently higher quality than oblique images, mainly due to reduced distortions, uniform lighting conditions, and consistent focus. Image quality ratings in all datasets were typically above 0.74, except in May 2024, when the lowest value was 0.31. In this case, we retained slightly blurry images due to their clustering and coverage of critical parts of the cliff face. Overall image overlap was ample.

Confidence values indicate the number of depth maps used for generating one point in the point cloud (Fig. 5). Depth maps are calculated when two images share over 100 matching points. Combined depth maps for one camera are transformed into a partial point cloud and merged into a dense point cloud. Therefore, lower confidence values are generally located in the model border areas and on rapidly changing or partially hidden surfaces, such as the back wall and bottom of small notches and the hidden bottoms of lower limestone layers.

Reprojection error is used to evaluate the accuracy of 3D reconstruction. It is the distance between the point in the image onto which a reconstructed 3D point is projected and the original point in the image that was used to detect and reconstruct the 3D point. The reprojection error in all models remained within 0.48–1.64 pixels, suggesting that the camera

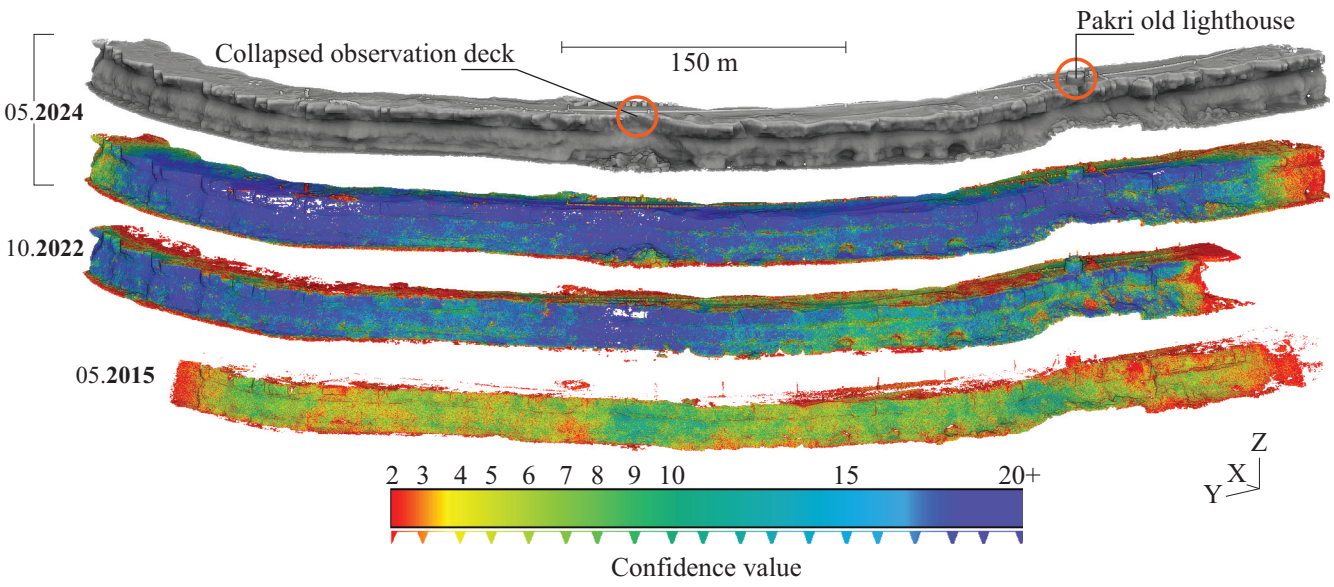


Fig. 5. Distribution of confidence values across point clouds. Values below 2 have been removed to improve accuracy.

parameters and calibration were reliable. The average camera location error was calculated using the RMSE for the axis coordinate across all camera locations, reflecting the discrepancy between the initial GNSS-log positions and the optimised camera coordinates derived from bundle adjustment. The high mean camera position error in May 2024 is likely a consequence of the non-functioning RTK system, which might have led to false absolute positioning of the model. Despite this, the overall geometry and relative accuracy of the model were preserved thanks to a sufficient number of tie points and projections.

The visual quality of the photogrammetric models improved over the years due to the increasing number of high-quality images. Water level, active ripples, and talus blocks limited flight level elevation in the lower section, slightly affecting the quality of the point cloud and mesh texture. Due to the significant geometric variability of the notches, the ceilings and trailing edges of most shallow and deep notches remained unmapped. Although the quality of the models varied over the years, it was sufficient for spatial comparison, change detection, and structural analysis.

3.3. Geological and structural interpretation

The photogrammetric models were imported to Virtual Reality Geological Studio (VRGS) for geological interpretation. The geological strata were segmented based on colour and texture gradients, in addition to the logic of the composite section. The upper ~7 m of Middle Ordovician carbonates were mapped as a single rock body due to poor visibility of thin layers and continuous fracturing throughout the entire rock body. In talus-covered areas, strata boundaries were not defined.

Joint systems were found throughout the entire rock body, but they were most prominently observed in limestone. Coplanarity, curvature change, and dip attributes were evaluated, and joint planes were fitted using at least three anchor points to minimise occasional irregularities. Orientation and dip were determined using the Dip Azimuth tool for planes. Orientation data were visualised using Stereonet v11 and clustered and analysed with Orient v3.24.

Measuring the morphometric parameters of coastal notches proved to be challenging, as they vary in shape and size. Four key parameters were measured: width, depth, height, and azimuth (Fig. 6). Width was defined as the straight-line horizontal distance between the outermost points of the notch mouth. Depth was measured as the distance from the midpoint of the notch mouth to the deepest part of the notch (retreat point), with azimuth measured along the depth axis. The height of the notch was measured vertically from the lower boundary of the black shale to the highest peak of the notch roof. The shale boundary was used as a stable reference surface to avoid distortion caused by the accumulation of loose sediment or floor irregularities.

3.4. Change detection

Orthophotos were used for the detection and mapping of long-term cliff edge retreat along an approximately 800-m section of Pakri Cliff, representing the area most directly exposed to wave action. The Republic of Estonia Land and Spatial Development Board (2025) provides open-access aerial photos, with historical images (1939–1993) available in the digital archive and contemporary images in the Geoportal. Unlike modern GeoTIFFs, historical orthophotos were available only as JPGs; consequently, their spatial resolution was derived from the post-georeferencing cell size. A total of three photos of the Pakri Peninsula from before the turn of the century were available, from 1959 (resolution 1.6 m), 1992 (0.4 m), and 1998 (0.75 m). Photos from 2010, 2020, and 2024 (0.2–0.25 m) were also included. While technical constraints play an important role, the digitisation of features such as cliff edges remains a subjective task, as it depends on feature recognition and individual interpretation. To minimise uncertainty, the cliff edges for all years were vectorised in ArcGIS Pro 3.2 at an approximate scale of 1:300. The retreat rate was calculated in total and compared with previous years.

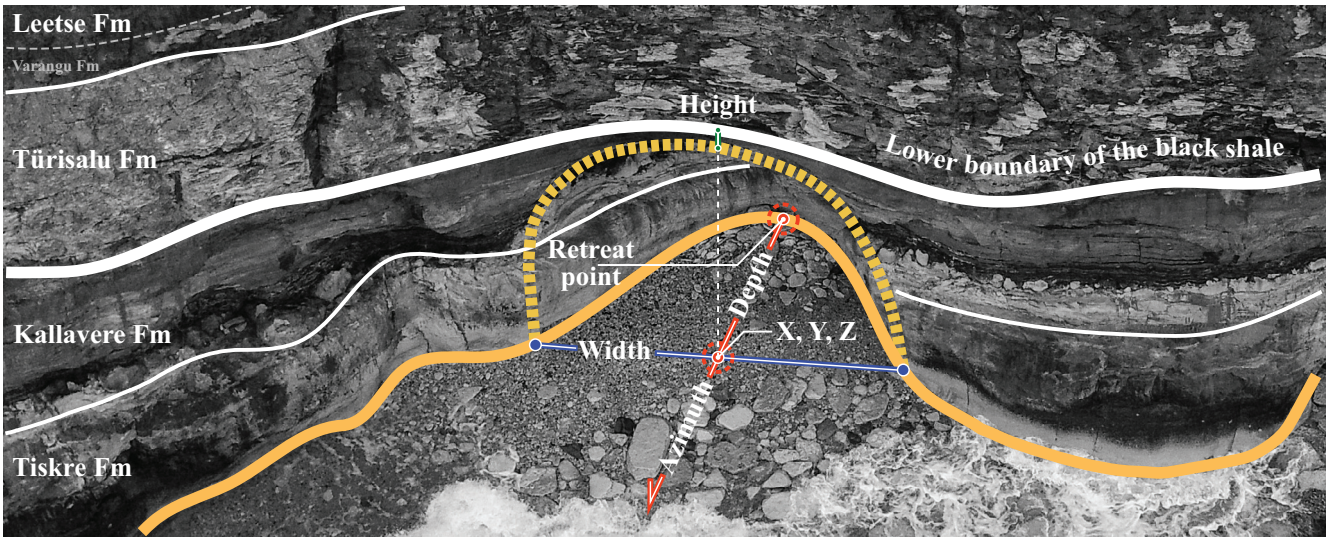


Fig. 6. Visualisation of the measured morphometric parameters of a coastal notch. The X, Y, and Z coordinates represent the midpoint of the notch mouth.

For volumetric and cliff-face analyses, the study area was limited to a 525-m subsection to ensure spatial consistency with the shorter extent of the 2015 model. To detect morphological changes, the point clouds from 2015, 2022, and May 2024 were imported into CloudCompare v2.13.2. Thereupon, all models were georeferenced and refined by removing duplicate points, statistical outliers, and low-confidence points. The multiscale model-to-model cloud comparison (M3C2) tool was employed to calculate changes in the cliff face.

The methodology for volumetric change was adapted from Doran et al. (2026). The cliff face was divided into five relatively even segments, followed by horizontal sectioning and alignment with the reference axis. Finally, the data were processed using the Compute 2.5D Volume tool, with a grid step size of 1 m. When determining layer transitions, a buffer of approximately 10–15 cm was used. Uncertainty thresholding was implemented using the level of detection, calculated as $LoD_{95\%} = 1.96 \times S_{stratum} \times (RMSE + 0.02\ \text{m})$, where 1.96 corresponds to the 95% confidence interval under a normal distribution, $S_{stratum}$ is an area-based scaling factor, and $RMSE$ + 0.02 m is the combined error incorporating the model alignment offset and residual noise buffer.

4. Results

4.1. Structural mapping

Geological strata boundaries can be clearly distinguished by their colour, texture, and consistent thickness in the dimensions of the entire model. Mapping the Varangu Fm (thickness ~0.5 m), beneath the glauconitic silts and sandstones, proved impossible due to the downward creep of greenish-grey glauconite, obscuring the lower layers, and marginal texture difference. Generally, the average stratum thickness was similar to that depicted in Fig. 2.

Smooth fracture surfaces representing vertical joint systems were observed in all mapped formations except in Leetse Fm, where they remain hidden due to the relatively soft and friable rock (Fig. 7). It is noteworthy that faults were identified in nearly all strata; however, tracing these faults throughout the full vertical extent proved challenging, as the joints did not visually penetrate all layers. Stereogram analyses, based on plane density, revealed dominant NW–SE and NE–SW joint sets in the cliff face, confirmed by point-girdle-random (PGR) analyses, which indicated the distribution of points within each orientation set and enabled k-means clustering. The proportion of mapped surface orientations was relatively even, with a slight predominance of the NW–SE set at 55% compared with 45% for the NE–SW set, suggesting the absence of a visually discernible dominant joint set. The calculation of the average direction of the joints in the whole vertical section was complicated by their substantial dispersion in the dominant orientations, leading to broad confidence intervals for the mean orientation vector. Therefore, maximum eigenvectors were calculated to quantify pole density and statistically describe the average orientation. Minimum eigenvectors would have been located in the middle of the sphere, as most of the mapped surfaces remained within the slope range of 70–90°. The average strike of the NW–SE joint set was 324° ± 2.5°, and that of the NE–SW set was 55° ± 3.6°.

Whereas spherical stereonets depict joint orientations and dip, density maps visualise the geographical location and distribution of these features. Joint density was evaluated based on fractures mapped in the limestone blocks due to being outlined and visually observed along the total survey section (Fig. 8). However, it is important to note that only fractures with a clear and recognisable surface were mapped, and the overall fracture network in both directions may be significantly more extensive. Assessing the fracture apertures proved difficult, as they were either not present or could not be detected in the model.

The spatial distribution of the fractures exhibits some variability along the coast. While NW-oriented fractures are relatively evenly distributed across the section, with occasional areas of higher concentration, the NE set exhibits a denser and more clustered pattern.

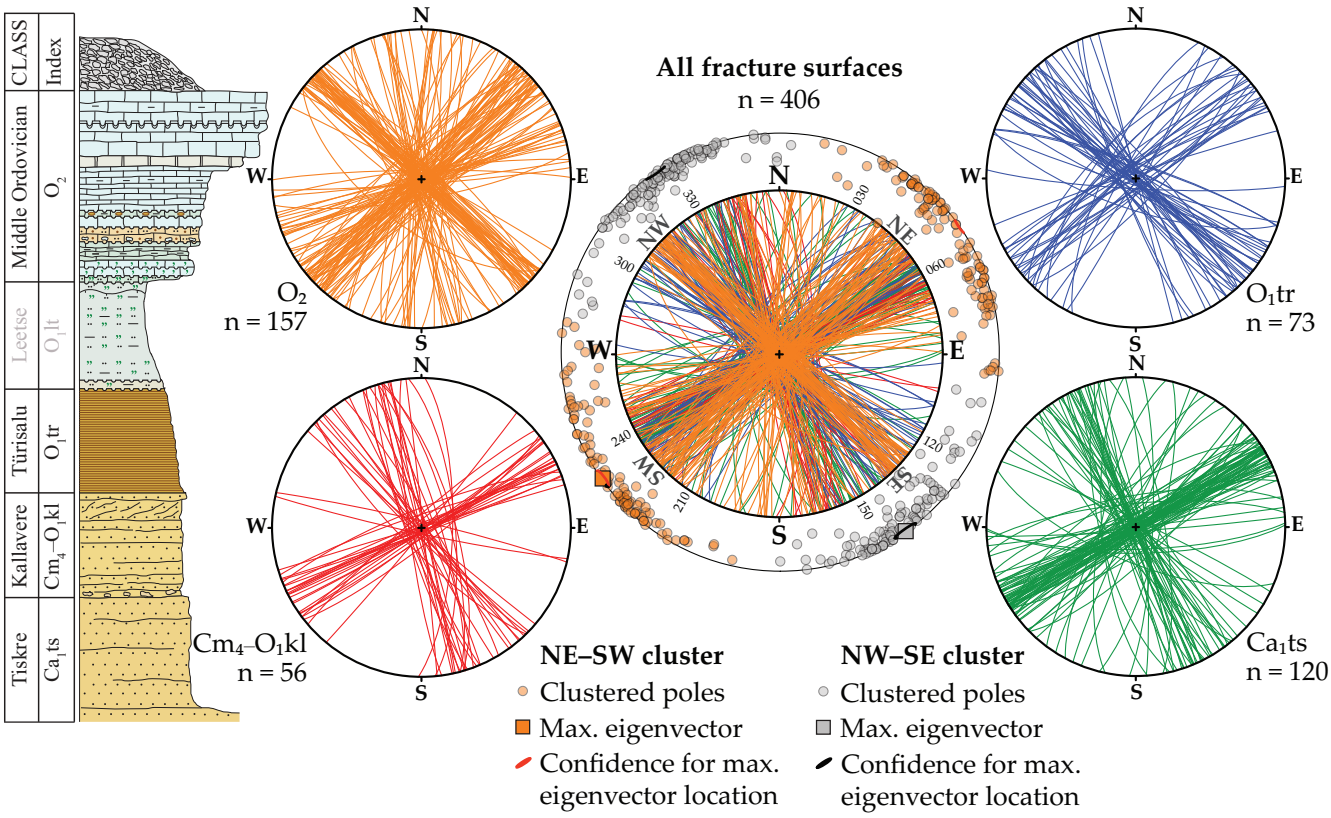


Fig. 7. Stereonets of mapped fracture surfaces, with clustered orientations plotted as poles. Projected on an equal-area lower hemisphere.

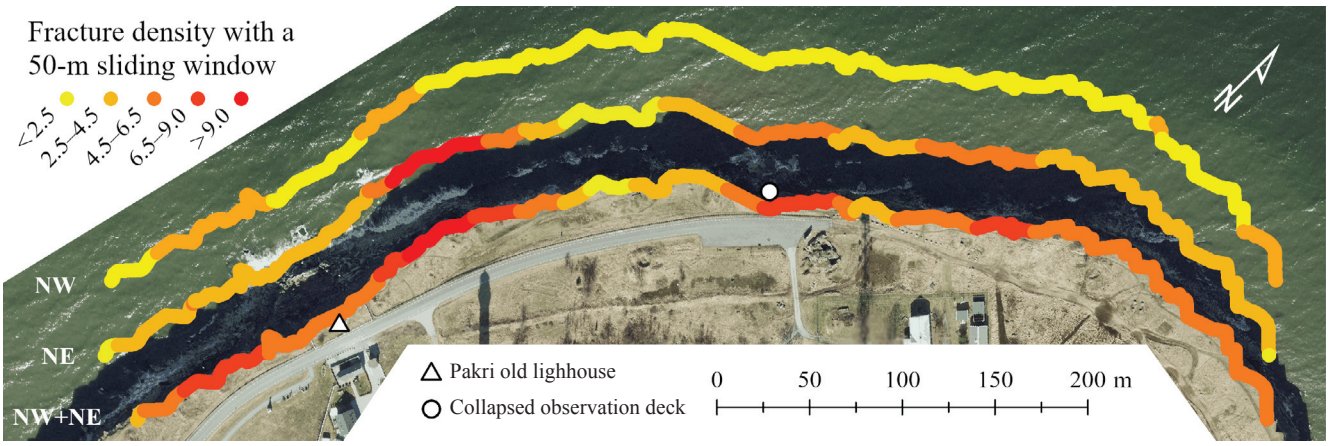


Fig. 8. Fracture density in Middle Ordovician carbonates within a 50-m sliding window, with separate profiles for NW-oriented, NE-oriented, and all joint sets.

Coastal notches, mapped from the May 2024 model, exhibit a wide range of shapes and sizes, varying from small and shallow indentations to pronounced cavities several metres wide and deep. Along an 800-m-long cliff edge, of which approximately 200 m is protected and obscured by fallen talus, a total of 18 notches and 19 horizontal V-shaped indentations, which appear to represent an early stage of notch formation (proto-notches), were mapped (Fig. 9).

Coastal notches have mainly developed within the weakly cemented, aleurite-rich Tiskre Fm, and have been primarily shaped by wave abrasion. They extend slightly into the conglomerate layer at the base of the overlying Kallavere Fm. In a few instances, where the conglomerate is thicker, the notches exhibit step-like incision patterns, indicating differential erosion. Notches in more advanced stages of development extend up to the black shale but have not penetrated it. In general, notch depth tends to increase with height, and wider notch mouths are linked to greater incision depth and height. The spatial distribution of notches and proto-notches is concentrated in two clusters, each approximately 200 m in length. The first is located between the old lighthouse and the collapsed observation deck, with predominantly NW-oriented, high and deep features, and the second extends about 100 m further, ending at the eastern boundary of the study area where shallower N- and NE-oriented features dominate. The morphometry and orientation of the retreat point indicate that most of the formations may have been initiated by intersecting fracture systems (Fig. 8).

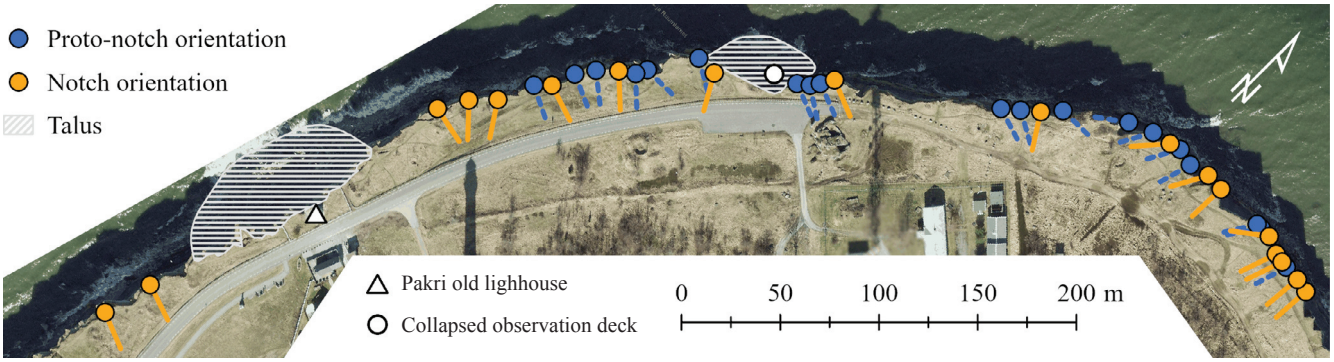


Fig. 9. Distribution and orientation of coastal notches and proto-notches.

4.2. Change detection

4.2.1. Cliff edge retreat

Using available orthophotos, the cliff edge was mapped for six different years over a 65-year period (Fig. 10). Georeferencing the earlier images was difficult due to a lack of unambiguous reference points, photo manipulations in military areas, low spatial resolution, or internal distortions. The alignment was evaluated at several points along the cliff edge, with deviations generally ranging from 20 to 35 cm, which were considered sufficient for the analysis of long-term coastal changes.

Orthophoto analysis covering the period 1959–2024 indicates a cumulative cliff edge retreat of approximately 9670 m^2, consisting of discrete rockfalls in the upper section. Major collapse events reported in the media during this century include the collapse of the observation deck (~240 m^2) on 16 January 2024, the detachment of a limestone block (~10 m^2) near the old lighthouse, damaging part of the footpath, on 22 April 2021, and multiple substantial failures (~1050 m^2) between 2–4 March 2008, which removed a large section of the cliff and reached the foundation of the historic lighthouse.

Between 1959 and 1992, spanning 33 years, the retreat was relatively uniform, amounting to 5600 m^2, with the zigzag morphology of the eastern cliff section highlighting the influence of diaclase systems on rockfall dynamics. The shorter interval from 1992 to 1998 introduced potential inaccuracies in georeferencing, as evidenced by intersecting cliff edges, rendering precise measurements of retreat uncertain; however, collapses during this time likely affected an estimated area of 250 m^2 in the eastern cliff section. A more pronounced retreat occurred between 1998 and 2010, with a total area loss of 2290 m^2, primarily concentrated near the Pakri old lighthouse, the collapsed observation deck, and the adjoining areas. During the subsequent decade (2010–2020), the cliff exhibited relative stability, with a reduced retreat of 870 m^2, although localised changes were noted along the zigzag edges in the eastern and western sections. In the current decade (2020–2024), ongoing processes, including the collapse of the observation deck, have resulted in an additional retreat of 650 m^2.

The cliff edge length, as determined from the 2024 orthophoto, is 810 m. Comparing the first and last orthophotos, spanning 65 years, the linear retreat rate is 18 cm/year. Between 1992 and 2024 (32 years), the rate is 16 cm/year, and between 2010 and 2024 (14 years), it is 13 cm/year. The arithmetic mean of the three results is 16 cm/year, while the weighted mean is 17 cm/year. The most significant erosion has been observed near the Pakri old lighthouse and the collapsed observation deck, where the estimated rate reaches 30 cm/year. In other areas, the rate of erosion is comparatively lower.

4.2.2. Cliff face retreat

During the study, three general erosion-accumulation models were generated using dense point clouds (Fig. 11), representing changes over the periods 2015–2022, 2022–2024, and 2015–2024. The most significant changes in the 2022 model, compared with 2015, were observed approximately 40 m southeast of the collapsed observation deck, 15 m north of

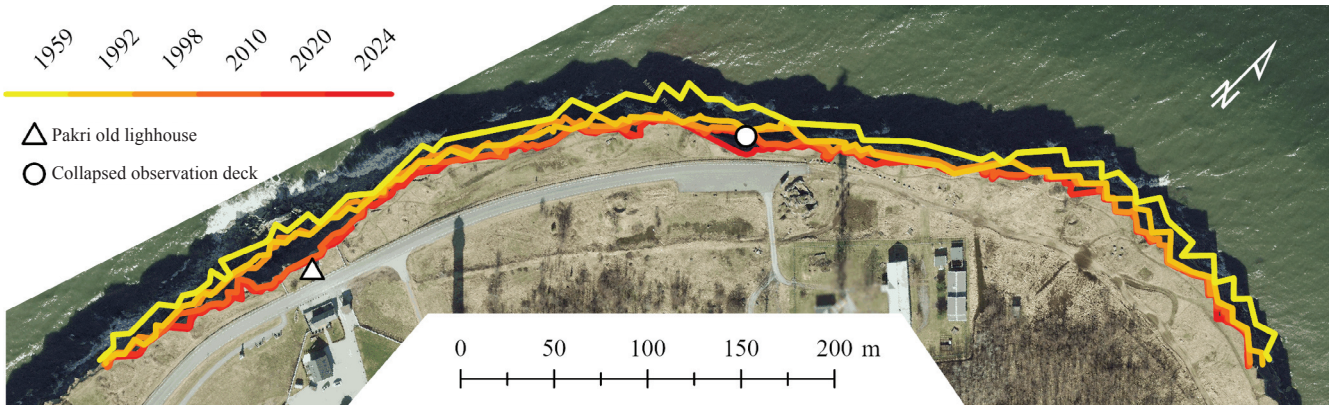


Fig. 10. Cliff edge retreat over 65 years.

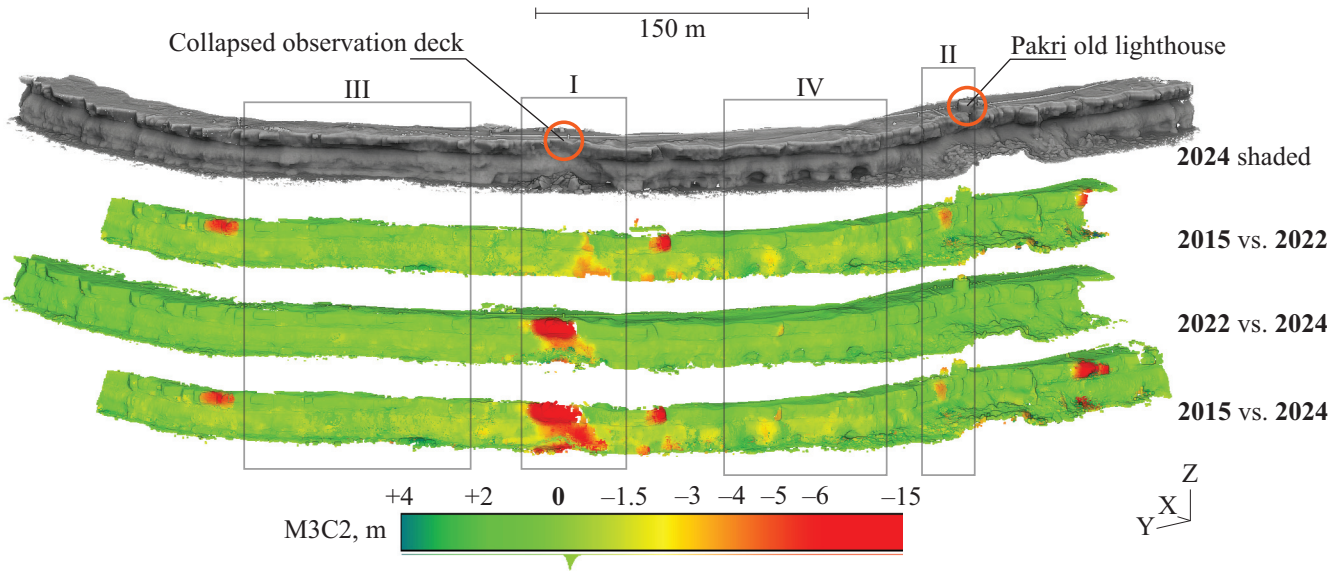


Fig. 11. Changes in a section of the cliff face over time. I – location of the collapsed observation deck, II – collapse of the limestone block, III – retreat of glauconitic sandstone, IV – notches. Abbreviation: M3C2 – model-to-model cloud comparison.

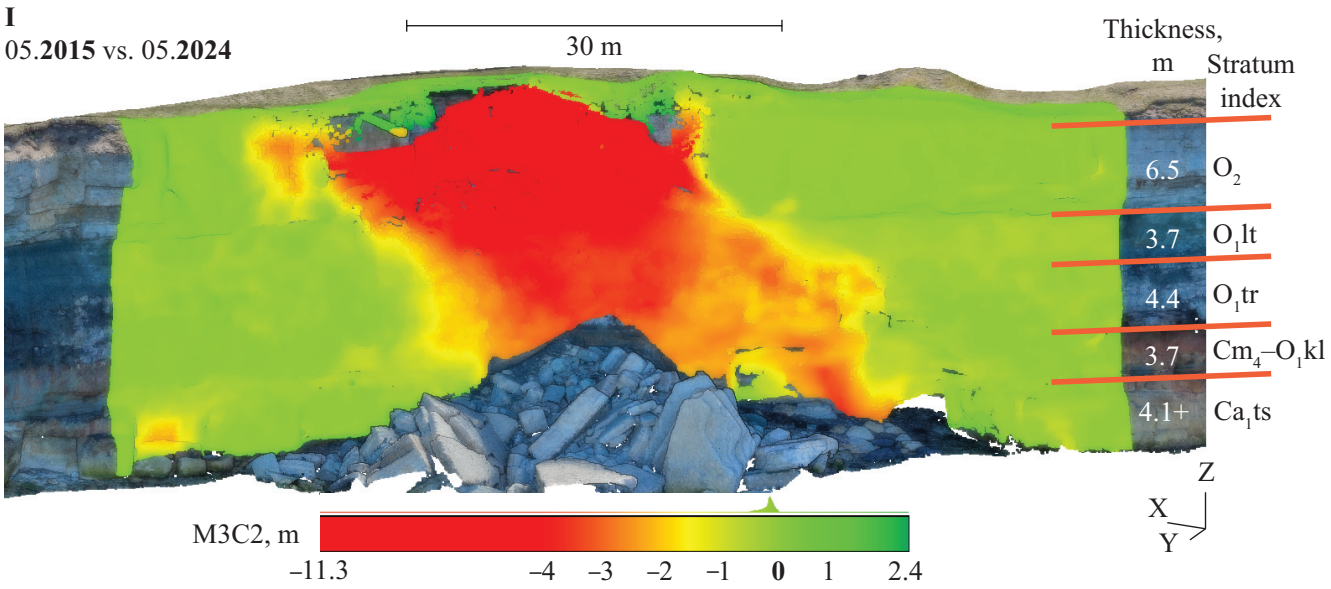


Fig. 11A. Section I – changes associated with the collapse of the Pakri observation deck.

the old lighthouse, and in the southern section of the zigzag cliff edge. Furthermore, a significant collapse is partially visible near the model's edge, approximately 70 m from the old lighthouse; however, the 2022 model is shorter than the others, and the full extent of the collapse is not entirely apparent, but it is still visible in the 2015–2024 model. The most significant change in 2024 compared with 2022 occurred at the location of the observation deck that collapsed in January 2024.

Models were examined in more detail at four different locations along the cliff face. Firstly, the most significant change over the years was the collapse of the observation deck on 16 January 2024 (Fig. 11A). The collapse affected a 30-m section, resulting in cliff face retreat of 12 m. Total loss of material was around 2800 m^3, of which at least approximately half was limestone. In front of the cliff, a nearly 5-m-high talus formed, acting as a protective barrier.

Secondly, on 22 April 2021, a block of limestone nearly 10 m wide collapsed next to the old lighthouse (Fig. 11B). The collapse of the approximately 340 m^3 block caused a cliff edge retreat of nearly 3 m. The height of the talus increased by around 4.5 m.

Thirdly, changes in the more friable rocks beneath the Ordovician strata were compared (Fig. 11C). Unlike limestones, which fall in blocks, the regression of sandstone has been relatively continuous and uniform throughout the cliff. There has been less loss in locations where the debris slope has protected the cliff toe from waves. In contrast, fine sandstone sediments are immediately washed away and do not form talus.

Finally, the abrasion notches were examined (Fig. 11D). No major collapses had occurred within the coastal notches. However, approximately one metre or more of material from the bottom of the notches had been washed away and replaced

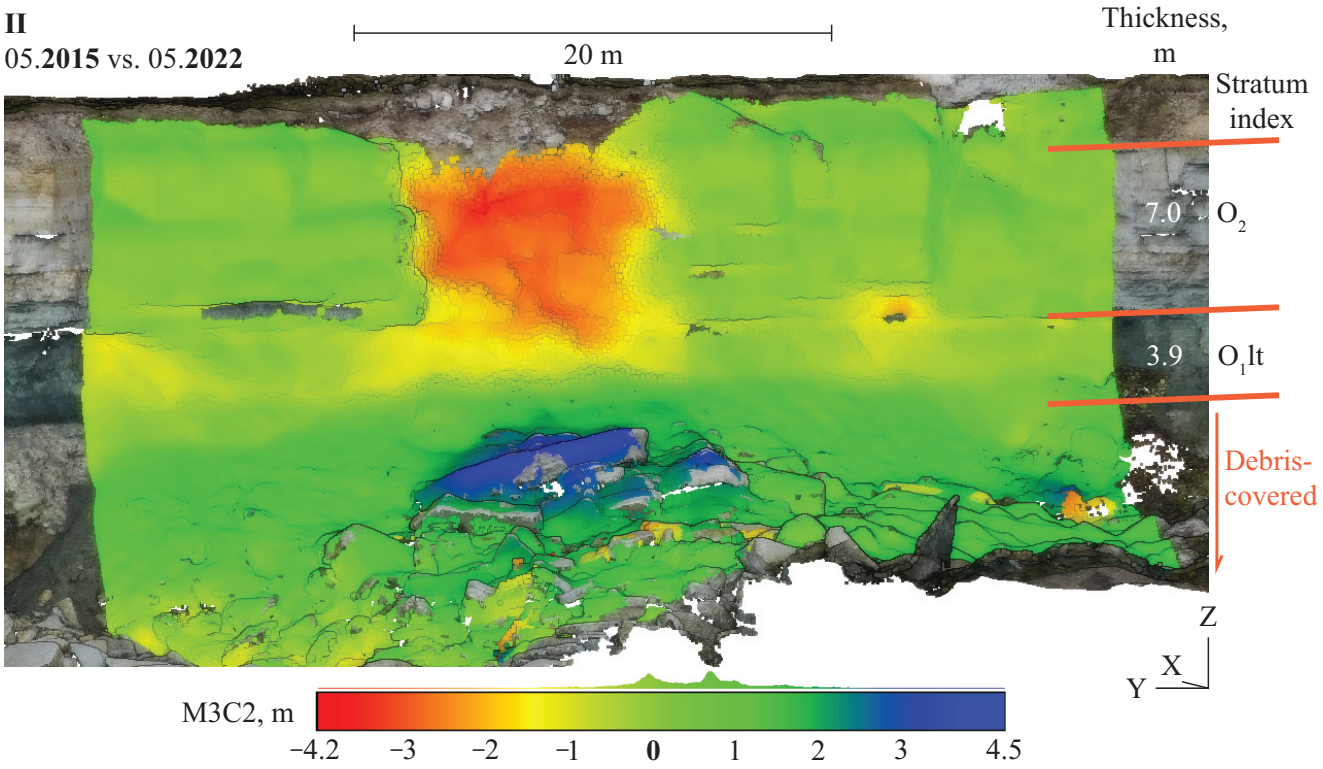


Fig. 11B. Section II – collapse of a limestone block next to the Pakri old lighthouse.

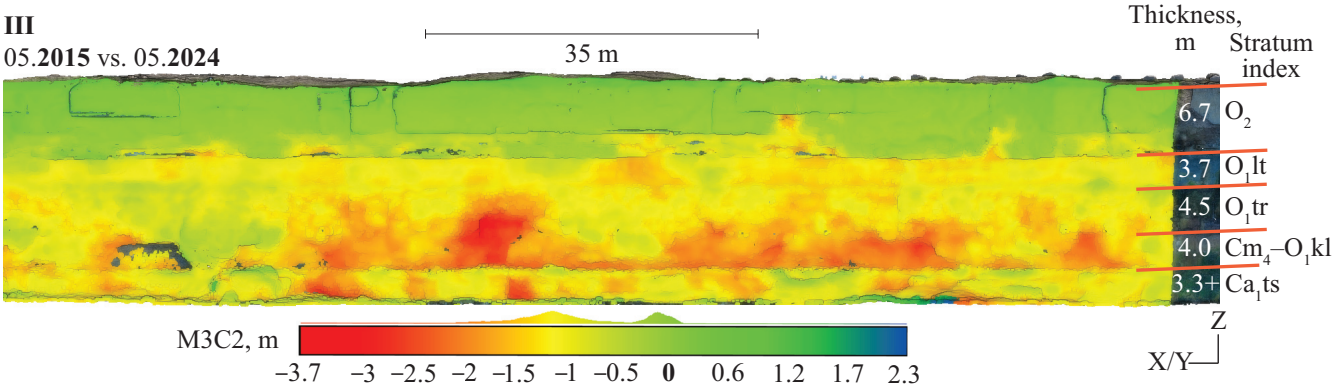


Fig. 11C. Section III – retreat of lower sandstone.

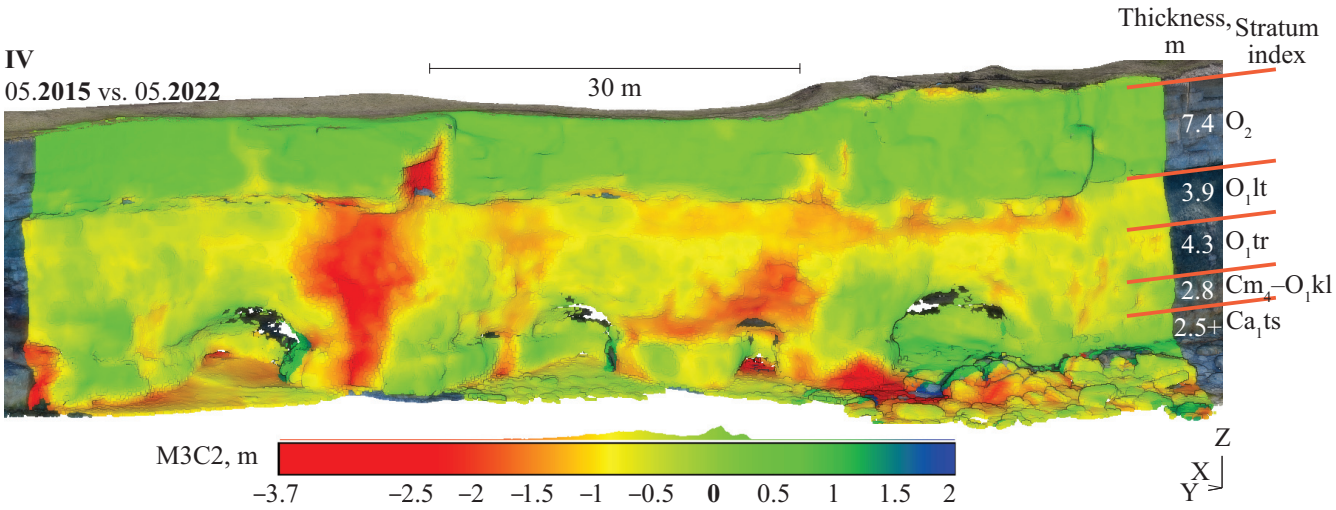


Fig. 11D. Section IV – coastal notches.

Table 2. Retreat rates and volumes by stratum class

Stratum class	Average layer thickness, m	Measured volume of eroded material (2015–2024), m^3	Measured/total surface area, m^2	Median retreat rate, m/year	Average retreat rate, m/year
Middle Ordovician	6.8	3911 ± 348	3550/3570	0.10 ± 0.05	0.14 ± 0.05
Leetse	4.0	1816 ± 186	1898/2100	0.10 ± 0.05	0.11 ± 0.05
Türisalu	4.3	1797 ± 206	2100/2258	0.08 ± 0.05	0.10 ± 0.05
Kallavere	3.6	1154 ± 145	1476/1890	0.08 ± 0.05	0.09 ± 0.05
Tiskre	3.5	698 ± 97	990/1837	0.07 ± 0.05	0.10 ± 0.05
Compared section, 525 m		9376 ± 981	10 014/11 655		

by finer-grained sediment. In more protected areas, sediment loss was significantly lower.

From 2015 to 2024, the 525-m section of the cliff lost a total volume of 9376 ± 981 m^3, translating to an average annual loss of approximately 1040 m^3. The retreat rates and volumes for each stratum class are detailed in Table 2. Although individual lithological units have different mean annual retreat rates, large-scale collapse events reset these differences by removing multiple layers simultaneously. The resulting freshly exposed cliff face is initially relatively even, but variations in lithological resistance cause differential retreat over time, leading to an increasingly irregular vertical profile.

4.3. Conceptual model of Pakri Cliff processes and future predictions

The conceptual model synthesises the geomorphological and environmental factors that drive cliff retreat (Fig. 12).

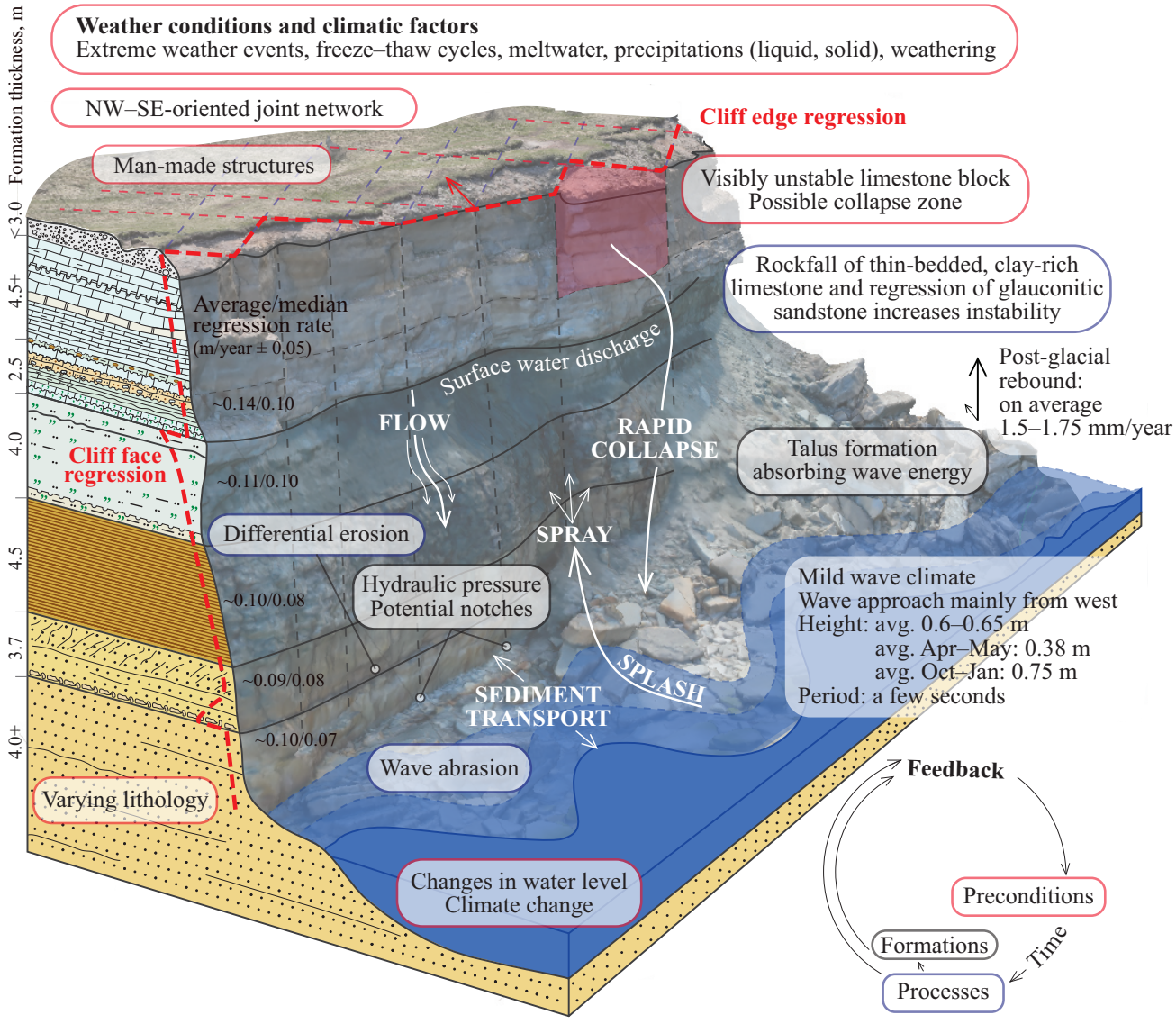


Fig. 12. Conceptual model of Pakri Cliff retreat. Average wave climate characteristics are adapted from Soomere and Räämet (2011), and the land uplift rate relative to the geoid is based on the NKG2016LU_lev model (Suursaar and Kall 2018; Vestøl et al. 2019). A detailed overview of the relevant processes, controls, scales, and feedbacks is presented in Table 3.

Pakri Cliff is characterised by rapid rockfall in the limestones, gradual regressive weathering in the middle sandstone, and slow wave erosion below. Rockfall is controlled by joint systems and promoted by weather conditions such as freeze–thaw cycles and precipitation, as well as being triggered by mass movement. In areas with denser intersections of joints – such as near the collapsed observation deck and the old lighthouse – cliff retreat has been somewhat faster, likely due to additional stress from near-edge structures. In the Leetse Fm, regression is constant, slowing down during the colder season, when liquid precipitation is less abundant. Rainwater infiltrating through jointed limestones and discharging above erodible layers acts as one of the key agents of erosion.

The lower section of the cliff, along with the upper strata during storm events, is influenced by active wave swash, splash, and spray. In addition to high wave intensity, hydraulic forcing within joints creates conditions favourable to the formation of abrasion notches. In the initial stage, the horizontal cross-section is V-shaped. As the notch deepens, mechanical erosion becomes more evenly distributed, leading to gradual rounding. Evolution is slow, and collapses are absent. Structural notches resulting from differential erosion have formed in the lower section of the Kallavere Fm, where the conglomerate weakens the structure. Talus, accumulated from collapses, provides an effective barrier against wave energy. While fine-grained material is transported seaward, larger boulders are difficult to move, remaining in place for decades. By altering morphometry, these processes feed back into and shape the dynamics that control ongoing development.

Geomorphic analysis, together with the evaluation of pre-failure conditions and mechanisms, supports the identification of potential failure zones (Fig. 13). For instance, before major collapses, including those of the observation deck and the limestone block, a significant retreat had already occurred in the glauconitic sandstone, thereby increasing the instability of the upper cliff section.

5. Discussion

5.1. Photogrammetric model as a cliff retreat monitoring tool

High-resolution UAV-SfM photogrammetry proved to be a robust approach for mapping and monitoring vertical and hard-to-reach cliff sections. Unlike traditional methods that fail to capture complex morphological changes beneath the cliff edge, SfM-MVS enables the volumetric quantification of sub-vertical surfaces and undercuts along the entire cliff face. Additionally, this approach facilitates detailed structural mapping across the cliff, which – when combined with layer-specific variations in retreat rates – helps identify potential rockfall zones.

Primary advantages over traditional methods include time and cost efficiency, as well as high spatial and temporal resolution when surveys are conducted across multiple flight campaigns. High-resolution models that preserve accurate geometric structure and detailed textural information facilitate comprehensive analysis of morphological features, including stratum thickness, surface characteristics, fault systems, and coastal notches. Moreover, quantitative comparison between successive models enables the detection and assessment of changes in the cliff face over time. Key challenges include data acquisition techniques, spatial consistency in quality, environmental factors, and processing resources, parameters, and optimisation (Gonçalves et al. 2021). While poor GNSS quality or the absence of GCPs limit direct georeferencing and require software-based scaling, aligning models with

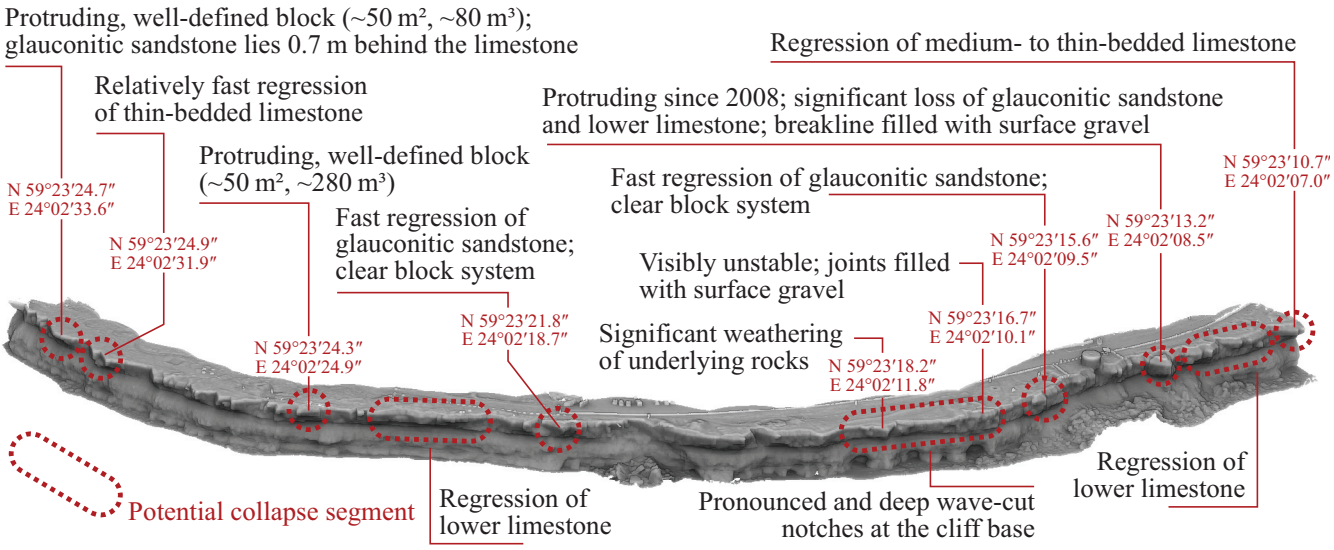


Fig. 13. Potential zones of cliff failure based on the authors' expert opinion.

Table 3. Processes driving Pakri Cliff retreat: controls, scales, and feedbacks

Process	Stratigraphic zone	Temporal regime	Structural/lithological control	Detachment unit / event volume	Detection method	Feedback (process, timescale)
Rockfall	Middle Ordovician carbonates (upper ~7 m)	Episodic, highly variable recurrence (annual to decadal scale); prepared by weathering and joint widening, triggered by pore-pressure events (rainfall, freeze, snowmelt)	NW–SE, NE–SW joint sets; near-edge stress; undermining by sandstone weathering	Blocks from 0.1 to >100 m^3 per event	Aerial-photo cliff-edge time series; 3D UAV-SfM time series (for volumes)	Event → forms talus (decadal shoreline protection) and resets the cliff's vertical profile to an even face
Mid-cliff subaerial weathering	Leetse glauconitic sandstone	Quasi-continuous; seasonally paced (freeze–thaw, wet–dry, seepage)	Lithology – poor cementation; seepage from jointed limestone above; marine spray	Grain-by-grain to flake-scale	3D UAV-SfM time series (sub-decimetric)	Undermines limestones above (years to decades) → prepares for rockfalls
Marine erosion / transport	Tiskre and Kallavere sandstones (base); storms occasionally impact upper layers	Seasonal with autumn–winter storm pulses; modulated by sea ice cover and talus shielding	Wave climate; joints initiating notches; weak conglomerate bed	Grain-scale notch deepening; episodic boulder removal	3D UAV-SfM analysis of notch morphometry; cliff-base bathymetry (currently missing)	→ removes talus shield (multi-decadal) → restores cliff-base wave abrasion

a single well-georeferenced base using persistent markers (e.g. artificial structures) can provide sufficient accuracy (Kong 2021). ICP-based referencing is effective when the transformation is based on a stable subset of the model and then applied to the entire dataset.

It must be noted that the spatial consistency of model accuracy is not uniform; reliability decreases at the model periphery and in areas where the image overlap is insufficient to capture the variability of the surface, for instance, in the steepest parts of the lower notches and in shaded spots where talus or the sea level limits flight elevation and visibility. Therefore, knowing the survey area and planning data collection are crucial for capturing important features. Ultimately, understanding these technical limits and optimisation strategies ensures that multi-temporal 3D datasets provide the geometric reliability required to accurately monitor and highlight the mechanisms driving cliff processes (Hayakawa and Obanawa 2020; Cirillo et al. 2024).

5.2. Process-based interpretation of cliff dynamics

The results show that cliff retreat at Pakri is controlled by an interplay of active swash processes, lithological preconditions, weathering, and structural joint systems, yielding a mean historical retreat rate of 18 cm/year (arithmetic mean: 16 cm/year; weighted mean: 17 cm/year). Extended periods of relative stability and little notable erosion are followed by significant rockfall episodes and general cliff edge retreat. Similarly, Orviku et al. (2013) found a comparable retreat rate (overall 25 cm/year; 20 cm/year without the March 2008 collapse) over 275 years. These figures highlight a remarkably high long-term retreat rate for Pakri Cliff, matching linear erosion rates more typical of much softer lithologies across the Baltic region. According to their study, regional cliff retreat rates depend heavily on geological composition: over a 240-year period, the more resistant limestone cliff of Osmussaare receded by only approximately 7 cm/year, whereas the soft Cambrian sandstone cliff at Kakumäe retreated by up to 60 cm/year according to repeated field measurements (1996–2006) and by approximately 80 cm/year based on orthophotos (1995–2010). Similar variance occurs along the southern Baltic Sea, where cliffs consist primarily of glacial and weakly lithified sedimentary rocks. For instance, cliffs composed of soft Pleistocene deposits in northern Germany, of broadly comparable height to Pakri, exhibit a mean retreat rate of 19 cm/year over 138 years (Averes et al. 2021), while glacial till cliffs on Wolin Island in northwestern Poland exhibit a comparable linear retreat rate of 14 cm/year over 30 years (Kolander et al. 2013). However, given that these till cliffs reach heights of up to 93 m – roughly three to four times the height of Pakri (~25 m) – the volumetric material loss there is likely substantially greater despite the similar linear rate; in this respect, erosion at Kakumäe, where comparably unconsolidated and highly erodible sediments are exposed, may be volumetrically more comparable to the Wolin till cliffs than to Pakri. Thus, erosion at Pakri Cliff is rapid and comparable, in linear terms, to rates observed in much softer geological formations, as it is controlled by the presence of highly erodible lithologies within the cliff profile. Table 3 provides a conceptual summary of the interactions between lithological zones, their respective temporal regimes, and the feedback mechanisms, illustrating a self-modulating geomorphic cycle.

Slope stability and rockfall are influenced by a combination of the geological setting and pre-failures, together with meteorological conditions (D'Amato et al. 2016), such as rainfall intensity and infiltration (Loew et al. 2022; Cirillo et al. 2024), temperature fluctuations (Gasc-Barbier et al. 2021), freeze–thaw cycles (Letortu et al. 2015), and storm-driven wave energy or swash that undercuts the cliff base. Within such a multi-mechanism system, it is challenging to give weights to different agents, since they usually occur in combination.

Structurally, these failures are heavily mediated by local joint systems, which coincide with the average transverse orientation observed in both the Paldiski locality and the broader Estonian bedrock (Thamm 1962; Miidel and Raukas 2005). The general orientation of the fractures suggests that they are part of a diagonal complex; however, the predominant NW trend is somewhat diffuse to the north and could be divided into two subclusters. The average orientation in the Middle Ordovician carbonates and the Türisalu Fm is around 315°, while that in the Kallavere and Tiskre Fms is 332°. A similar tendency was noted by Teichert (1927) in the Toila locality, where diagonal joints are more common in carbonates and orthogonal joints in sandstones. According to Sokman et al. (2008), fracture density varies significantly between locations and can also be influenced and densified by glaciotectonic stress and deformation near pre-weakened fault zones (Rattas and Kalm 2004). The NE-oriented joint system, based solely on fractures in the Middle Ordivician strata, is distinctly denser, with surfaces forming a substantial part of the cliff face. It is important to critically assess the joint-density estimates in the area, as it is based solely on joints visible at the surface. For instance, joint density can be specified using ground-penetrating radar (Pipan et al. 2003; Deparis et al. 2007).

5.3. Implications for geohazard assessment

As a geotourism destination, Pakri Cliff requires robust and continuous monitoring, with the characterisation of the multi-mechanism nature of erosion being of direct practical relevance to geohazard mitigation. Because cliff evolution is inherently non-linear and heavily influenced by episodic, high-magnitude events, relying solely on simplified linear projections or historical averages can lead to underestimating short-term geohazards. The SfM-MVS-based 3D models demonstrate that tracking cliff face dynamics can successfully identify locations of structural asymmetry and undercutting before major failures occur. Furthermore, the ability of the UAV-SfM workflow to safely map vertical, otherwise inaccessible sections provides local municipalities with the empirical data needed to delineate safety buffer zones, protect public infrastructure, and manage traffic around high-risk zones.

6. Conclusions

Pakri Cliff retreated at an average rate of 18 cm/year between 1959 and 2024. Retreat is a complex process influenced by the geological setting, mass movement, weathering, meteorological factors, groundwater fluctuations, and wave action. Collapsed talus accumulates at the cliff base, providing partial protection and mitigating further erosion of the lower sections.

The study demonstrates that integrating high-resolution UAV-SfM photogrammetry with structural mapping provides a powerful framework for coastal monitoring and geohazard detection. This approach overcomes the limitations of traditional 2D mapping by providing higher accuracy and greater spatial coverage for detailed 3D analysis, which is critical for identifying processes and factors influencing the vertical cliff section.

While these 3D models offer an opportunity to identify contemporary coastal processes and conceptualise future evolution, precise long-term predictions remain extremely challenging. Erosion can vary significantly from year to year and is further influenced by the cliff's geometry and erosion characteristics. Incorporating the seaward component into the models is essential, as mapping the abrasion platform is critical to a comprehensive understanding of marine influences on coastal dynamics.

Data availability statement

The data collected and generated during this study are available from the corresponding author upon reasonable request. Orthophotos are publicly available via the Republic of Estonia Land and Spatial Development Board.

Acknowledgements

This study was supported by the Estonian Research Council (grant No. TemTA122). The publication costs of this article were partially covered by the Estonian Academy of Sciences.

Appendix

Table A1. General features of the drones used and camera specifications

Year	Drone	Drone specifications	Camera
2015	DJI Phantom 2 Vision	Net weight: 1160 g Diagonal length: 350 mm Georeferencing/hovering accuracy range: no official data	Gimballed RGB Sensor size: 1/2.3" Resolution: 14 MP Field of view: 110°
2022	DJI Phantom 4 RTK SDK	Net weight: 1360 g Diagonal length: 350 mm Georeferencing/hovering accuracy range: vertical: ±0.1 m (vision positioning enabled); ±0.5 m (GNSS positioning enabled); ±0.1 m (RTK enabled) horizontal: ±0.3 m (vision positioning enabled); ±1.5 m (GNSS positioning enabled); ±0.1 m (RTK enabled)	Gimballed RGB Sensor: 1" CMOS Resolution: 20 MP FOV: 84°
2024	DJI Mavic 3M	Net weight: 951 g Diagonal length: 380.1 mm Georeferencing/hovering accuracy range: vertical: ±0.1 m (vision positioning enabled); ±0.5 m (GNSS positioning enabled); ±0.1 m (RTK enabled) horizontal: ±0.3 m (vision positioning enabled); ±0.5 m (HD positioning enabled); ±0.1 m (RTK enabled)	Gimballed RGB and multispectral Sensor: 4/3 CMOS Resolution: 20 MP FOV: 84°

References

Adade, R., Aibinu, A. M., Ekumah, B. and Asaana, J. 2021. Unmanned aerial vehicle (UAV) applications in coastal zone management – a review. *Environmental Monitoring and Assessment*, **193**(3), 154. https://doi.org/10.1007/s10661-021-08949-8

Averes, T., Hofstede, J. L. A., Hinrichsen, A., Reimers, H.-C. and Winter, C. 2021. Cliff retreat contribution to the littoral sediment budget along the Baltic Sea coastline of Schleswig-Holstein, Germany. *Journal of Marine Science and Engineering*, **9**(8), 870. https://doi.org/10.3390/jmse9080870

Barba, S., Barbarella, M., Di Benedetto, A., Fiani, M., Gujski, L. and Limongiello, M. 2019. Accuracy assessment of 3D photogrammetric models from an unmanned aerial vehicle. *Drones*, **3**(4), 79. https://doi.org/10.3390/drones3040079

Berra, E. F. and Peppa, M. V. 2020. Advances and challenges of UAV SfM MVS photogrammetry and remote sensing: short review. In *2020 IEEE Latin American GRSS & ISPRS Remote Sensing Conference (LAGIRS), Santiago, Chile, 22–26 March 2020*. IEEE, 533–538. https://doi.org/10.1109/LAGIRS48042.2020.9285975

Calvin, K., Dasgupta, D., Krinner, G., Mukherji, A., Thorne, P. W., Trisos, C. et al. 2023. *Climate Change 2023: Synthesis Report.* IPCC, Geneva, Switzerland. https://doi.org/10.59327/IPCC/AR6-9789291691647

Cirillo, D., Zappa, M., Tangari, A. C., Brozzetti, F. and Ietto, F. 2024. Rockfall analysis from UAV-based photogrammetry and 3D models of a cliff area. *Drones*, **8**(1), 31. https://doi.org/10.3390/drones8010031

D'Amato, J., Hantz, D., Guerin, A., Jaboyedoff, M., Baillet, L. and Mariscal, A. 2016. Influence of meteorological factors on rockfall occurrence in a middle mountain limestone cliff. *Natural Hazards and Earth System Sciences*, **16**(3), 719–735. https://doi.org/10.5194/nhess-16-719-2016

Deliry, S. I. and Avdan, U. 2024. Accuracy assessment of UAS photogrammetry and structure from motion in surveying and mapping. *International Journal of Engineering and Geosciences*, **9**(2), 165–190. https://doi.org/10.26833/ijeg.1366146

Deparis, J., Garambois, S. and Hantz, D. 2007. On the potential of Ground Penetrating Radar to help rock fall hazard assessment: a case study of a limestone slab, Gorges de la Bourne (French Alps). *Engineering Geology*, **94**(1–2), 89–102. https://doi.org/10.1016/j.enggeo.2007.07.005

Dodge, S. E., Zoet, L. K., Rawling, J. E., III, Theuerkauf, E. J. and Hansen, D. D. 2022. Transport properties of fast ice within the nearshore. *Coastal Engineering*, **177**, 104176. https://doi.org/10.1016/j.coastaleng.2022.104176

Doran, T. A., Kennedy, D. M., McCarroll, J. R., Allan, B. M. and Ierodiaconou, D. 2026. Using UAV-derived point clouds to measure high resolution cliff dynamics in soft lithologies: Demons Bluff, Victoria, Australia. *Earth Surface Processes and Landforms*, **51**(4), e70285. https://doi.org/10.1002/esp.70285

Feng, C., Yu, D., Liang, Y., Guo, D., Wang, Q. and Cui, X. 2019. Assessment of influence of image processing on fully automatic UAV photogrammetry. *The International Archives of the Photogrammetry, Remote Sensing and Spatial Information Sciences*, **XLII-2/W13**, 269–275. https://doi.org/10.5194/isprs-archives-XLII-2-W13-269-2019

Gasc-Barbier, M., Merrien-Soukatchoff, V. and Virely, D. 2021. The role of natural thermal cycles on a limestone cliff mechanical behaviour. *Engineering Geology*, **293**, 106293. https://doi.org/10.1016/j.enggeo.2021.106293

Gonçalves, G., Gonçalves, D., Gómez-Gutiérrez, Á., Andriolo, U. and Pérez-Alvárez, J. A. 2021. 3D reconstruction of coastal cliffs from fixed-wing and multi-rotor UAS: impact of SfM-MVS processing parameters, image redundancy and acquisition geometry. *Remote Sensing*, **13**(6), 1222. https://doi.org/10.3390/rs13061222

Grimm, N. B., Chapin, F. S., III, Bierwagen, B., Gonzalez, P., Groffman, P. M., Luo, Y. et al. 2013. The impacts of climate change on ecosystem structure and function. *Frontiers in Ecology and the Environment*, **11**(9), 474–482. https://doi.org/10.1890/120282

Hayakawa, Y. S. and Obanawa, H. 2020. Volumetric change detection in bedrock coastal cliffs using terrestrial laser scanning and UAS-based SfM. *Sensors*, **20**(12), 3403. https://doi.org/10.3390/s20123403

Hints, O., Männik, P. and Toom, U. (eds) 2024. *XI Baltic Stratigraphical Conference, Abstracts and Field Guide*. Geological Society of Estonia, Tallinn. https://kirjandus.geoloogia.info/en/reference/49701 (accessed 2025-06-18).

Iglhaut, J., Cabo, C., Puliti, S., Piermattei, L., O'Connor, J. and Rosette, J. 2019. Structure from Motion photogrammetry in forestry: a review. *Current Forestry Reports*, **5**(3), 155–168. https://doi.org/10.1007/s40725-019-00094-3

Jaagus, J. and Suursaar, Ü. 2013. Long-term storminess and sea level variations on the Estonian coast of the Baltic Sea in relation to large-scale atmospheric circulation. *Estonian Journal of Earth Sciences*, **62**(2), 73–92. https://doi.org/10. 3176/earth.2013.07

James, M. R. and Robson, S. 2012. Straightforward reconstruction of 3D surfaces and topography with a camera: accuracy and geoscience application. *Journal of Geophysical Research: Earth Surface*, **117**(F3), F03017. https://doi.org/10.1029/2011JF002289

James, M. R., Chandler, J. H., Eltner, A., Fraser, C., Miller, P. E., Mills, J. P. et al. 2019. Guidelines on the use of structure-from-motion photogrammetry in geomorphic research. *Earth Surface Processes and Landforms*, **44**(10), 2081–2084. https://doi.org/10.1002/esp.4637

Jiang, S., Jiang, C. and Jiang, W. 2020. Efficient structure from motion for large-scale UAV images: a review and a comparison of SfM tools. *ISPRS Journal of Photogrammetry and Remote Sensing*, **167**, 230–251. https://doi.org/10.1016/j.isprsjprs.2020.04.016

Klemas, V. V. 2015. Coastal and environmental remote sensing from unmanned aerial vehicles: an overview. *Journal of Coastal Research*, **31**(5), 1260–1267. https://doi.org/10.2112/JCOASTRES-D-15-00005.1

Kolander, R., Morche, D. and Bimböse, M. 2013. Quantification of moraine cliff coast erosion on Wolin Island (Baltic Sea, northwest Poland). *Baltica*, **26**, 37–44. https://doi.org/10.5200/baltica.2013.26.04

Kong, X. 2021. Identifying geomorphological changes of coastal cliffs through point cloud registration from UAV images. *Remote Sensing*, **13**(16), 3152. https://doi.org/10.3390/rs13163152

Letortu, P., Costa, S., Cador, J.-M., Coinaud, C. and Cantat, O. 2015. Statistical and empirical analyses of the triggers of coastal chalk cliff failure. *Earth Surface Processes and Landforms*, **40**(10), 1371–1386. https://doi.org/10.1002/esp.3741

Letortu, P., Costa, S., Davidson, R., Maquaire, O., Peuziat, B., Thirard, G. et al. 2025. A decade of erosion monitoring of coastal chalk cliff faces at a seasonal frequency (2010–2021) using terrestrial lasergrammetry and photogrammetry (Varengeville-sur-Mer and Dieppe, Normandy, France): technical evolution and main results. *Geomorphology*, **479**, 109738. https://doi.org/10.1016/j.geomorph.2025.109738

Linder, W. 2009. *Digital Photogrammetry: A Practical Course*. 3rd ed. Springer, Berlin, Heidelberg.

Loew, S., Hantz, D. and Gerber, W. 2022. Rockfall causes and transport mechanisms – a review. In *Treatise on Geomorphology* (Shroder, J. F., ed.). Elsevier, 137–168. https://doi.org/10.1016/B978-0-12-818234-5.00066-3

Manson, G. K. 2022. Nearshore sediment transport as influenced by changing sea ice, north shore of Prince Edward Island, Canada. *Canadian Journal of Earth Sciences*, **59**(11), 935–944. https://doi.org/10.1139/cjes-2020-0150

Menier, D., Le Gall, R., Mathew, M. J., Sautter, B., Ramkumar, M., Ariffin, E. H. et al. 2025. Quantifying coastal cliff retreat, sediment volume, and dynamics using photogrammetry and geospatial analysis in the Pénestin Peninsula, France. *Geomorphology*, **482**, 109792. https://doi.org/10.1016/j.geomorph.2025.109792

Mens, K. and Puura, I. 1996. Pakri Peninsula. In *The Third Baltic Stratigraphical Conference. Abstracts. Field Guide* (Meidla, T., Puura, I., Nemliher, J., Raukas, A. and Saarse L., eds). University of Tartu Press, Tartu, 88–92.

Miidel, A. and Raukas, A. 2005. Slope processes at the North Estonian Klint. *Proceedings of the Estonian Academy of Sciences. Geology*, **54**(4), 209–224. https://doi.org/10.3176/ geol.2005.4.01

Miller, H. C. 1999. Field measurements of longshore sediment transport during storms. *Coastal Engineering*, **36**(4), 301–321. https://doi.org/10.1016/S0378-3839(99)00010-1

Najafzadeh, F. and Soomere, T. 2024. Impact of changes in sea ice cover on the wave climate of semi-enclosed, seasonally ice-covered water bodies at temperate latitudes: a case study in the Gulf of Riga. *Estonian Journal of Earth Sciences*, **73**(1), 26–36. https://doi.org/10.3176/earth.2024.03

Nicholls, R. J. and Cazenave, A. 2010. Sea-level rise and its impact on coastal zones. *Science*, **328**(5985), 1517–1520. https://doi.org/10.1126/science.1185782

Orviku, K., Tõnisson, H., Kont, A., Suuroja, S. and Anderson, A. 2013. Retreat rate of cliffs and scarps with different geological properties in various locations along the Estonian coast. *Journal of Coastal Research*, **65**(sp1), 552–557. https://doi.org/10.2112/SI65-094.1

Pipan, M., Forte, E., Guangyou, F. and Finetti, I. 2003. High resolution GPR imaging and joint characterization in limestone. *Near Surface Geophysics*, **1**(1), 39–55. https://doi.org/10.3997/1873-0604.2002006

Pryor, S. C., Barthelmie, R. J., Clausen, N. E., Drews, M., MacKellar, N. and Kjellström, E. 2012. Analyses of possible changes in intense and extreme wind speeds over northern Europe under climate change scenarios. *Climate Dynamics*, **38**(1), 189–208. https://doi.org/10.1007/s00382-010-0955-3

Rattas, M. and Kalm, V. 2004. Glaciotectonic deformation patterns in Estonia. *Geological Quarterly*, **48**(1), 15–22.

Republic of Estonia Land and Spatial Development Board. 2025. Geoportal. https://geoportaal.maaamet.ee/eng/ (accessed 2025-09-15).

Sokman, K., Kattai, V., Vaher, R. and Systra, Y. J. 2008. Influence of tectonic dislocations on oil shale mining in the Estonia deposit. *Oil Shale*, **25**(2S), 175–187. https://doi.org/10.3176/oil.2008.2S.09

Sooäär, J. and Jaagus, J. 2007. Long-term changes in the sea ice regime in the Baltic Sea near the Estonian coast. *Proceedings of the Estonian Academy of Sciences. Engineering*, **13**(3), 189–200. https://doi.org/10.3176/eng.2007.3.02

Soomere, T. 2024. Climate change and coastal processes in the Baltic Sea. In *Oxford Research Encyclopedia of Climate Science* (von Storch, H., ed.). Oxford University Press, Oxford. https://doi.org/10.1093/acrefore/9780190228620. 013.897

Soomere, T. and Räämet, A. 2011. Spatial patterns of the wave climate in the Baltic Proper and the Gulf of Finland. *Oceanologia*, **53**, 335–371. https://doi.org/10.5697/oc.53-1-TI.335

Soomere, T., Viška, M. and Eelsalu, M. 2013. Spatial variations of wave loads and closure depths along the coast of the eastern Baltic Sea. *Estonian Journal of Engineering*, **19**(2), 93–109. https://doi.org/10.3176/eng.2013.2.01

Suursaar, Ü. and Kall, T. 2018. Decomposition of relative sea level variations at tide gauges using results from four Estonian precise levelings and uplift models. *IEEE Journal of Selected Topics in Applied Earth Observations and Remote Sensing*, **11**(6), 1966–1974. https://doi.org/10.1109/ JSTARS.2018.2805833

Swirad, Z. M. and Young, A. P. 2025. Hazard of coastal cliff top failure through time. *Geomorphology*, **481**, 109791. https://doi.org/10.1016/j.geomorph.2025.109791

Teichert, C. 1927. Die Klufttektonik der cambro-silurischen Schichtentafel Estlands (Joint tectonics of the Cambrian–Silurian sedimentary sequence of Estonia). *Geologische Rundschau*, **18**(4), 241–263. https://doi.org/10.1007/BF01805276

Thamm, N. 1962. The horizontal displacement of the Island Osmussaar (Odinsholm) and the subsequence regeneration of normal rhegmatic jointing. *South African Journal of Geology*, **65**(2), 41–46.

Tõnisson, H., Suursaar, Ü., Orviku, K., Jaagus, J., Kont, A., Willis, D. A. et al. 2011. Changes in coastal processes in relation to changes in large-scale atmospheric circulation, wave parameters and sea levels in Estonia. *Journal of Coastal Research*, **57**, 701–705.

Turner, D., Lucieer, A. and Wallace, L. 2014. Direct georeferencing of ultrahigh-resolution UAV imagery. *IEEE Transactions on Geoscience and Remote Sensing*, **52**(5), 2738–2745. https://doi.org/10.1109/TGRS.2013.2265295

Tuuling, I., Bauest, H., Wilmann, S. and Budd, G. E. 2011. *The Baltic Sea: Geology and Geotourism Highlights*. GeoGuide Baltoscandia, Tallinn.

Vestøl, O., Ågren, J., Steffen, H., Kierulf, H. and Tarasov, L. 2019. NKG2016LU: a new land uplift model for Fennoscandia and the Baltic Region. *Journal of Geodesy*, **93**, 1759–1779. https://doi.org/10.1007/s00190-019-01280-8

Walsh, J. E., Ballinger, T. J., Euskirchen, E. S., Hanna, E., Mård, J., Overland, J. E. et al. 2020. Extreme weather and climate events in northern areas: a review. *Earth-Science Reviews*, **209**, 103324. https://doi.org/10.1016/j.earscirev.2020.103324

Wang, S., Ahmed, Z., Hashmi, M. Z. and Pengyu, W. 2019. Cliff face rock slope stability analysis based on unmanned arial vehicle (UAV) photogrammetry. *Geomechanics and Geophysics for Geo-Energy and Geo-Resources*, **5**(4), 333–344. https://doi.org/10.1007/s40948-019-00107-2

Weisse, R., Dailidienė, I., Hünicke, B., Kahma, K., Madsen, K., Omstedt, A. et al. 2021. Sea level dynamics and coastal erosion in the Baltic Sea region. *Earth System Dynamics*, **12**(3), 871–898. https://doi.org/10.5194/esd-12-871-2021

Westoby, M. J., Brasington, J., Glasser, N. F., Hambrey, M. J. and Reynolds, J. M. 2012. 'Structure-from-Motion' photogrammetry: a low-cost, effective tool for geoscience applications. *Geomorphology*, **179**, 300–314. https://doi.org/10.1016/j.geomorph.2012.08.021

Wolski, T. and Wiśniewski, B. 2021. Characteristics and long-term variability of occurrences of storm surges in the Baltic Sea. *Atmosphere*, **12**(12), 1679. https://doi.org/10.3390/atmos12121679

Young, A. P., Flick, R. E., Gutierrez, R. and Guza, R. T. 2009. Comparison of short-term seacliff retreat measurement methods in Del Mar, California. *Geomorphology*, **112**(3–4), 318–323. https://doi.org/10.1016/j.geomorph.2009.06.018

Zaitseva-Pärnaste, I., Suursaar, Ü., Kullas, T., Lapimaa, S. and Soomere, T. 2009. Seasonal and long-term variations of wave conditions in the Northern Baltic Sea. *Journal of Coastal Research*, **56**(1), 277–281.

Pankranniku erosiooniprotsesside ja georiskide kaardistamine 3D-modelleerimise abil Pakri panga näitel

Tiia-Linda Purge, Marko Kohv, Martin Liira ja Tiina Harak

Ortofotode analüüsi põhjal on Pakri pank ajavahemikus 1959–2024 taandunud keskmiselt 18 cm aastas. Panga taandumine on kompleksne protsess, mida kujundab mitme teguri koosmõju, sealhulgas geoloogiline ehitus ja eeltingimused, murenemine, meteoroloogilised tegurid, põhjaveerežiim, massiliikumised ning panga jalamil toimuv murrutus. Erosiooni kiirus ja iseloom sõltuvad litoloogiast. Suuremad keskmised ja mediaansed taganemiskiirused esinevad Ordoviitsiumi lubjakivides (keskmine 14 ± 5 cm/a, mediaan 10 ± 5 cm/a) ja Leetse glaukoniitliivakivides (keskmine 11 ± 5 cm/a, mediaan 10 ± 5 cm/a), millest viimased on nõrgalt tsementeerunud ja mille pinnalt toimub maapinda infiltreerunud vee väljavool. Alumine osa, sh Türisalu must kilt ning Kallavere ja Tiskre liivakivid, taganeb mõnevõrra aeglasemalt, ent on oluliselt mõjutatud kukkuvatest lubjakiviplokkidest, mis võivad endaga kaasa haarata terve läbilõike. Kuigi ülemiste lubjakivide taandumine on pikas perspektiivis pigem episoodiline ja muutliku kordusintervalliga, on see visuaalselt hästi eristatav, kuna varinguid kontrollivad enamasti loode–kagu- ja kirde–edelasuunalised aluspõhjakivimeid läbivad vertikaalsed lõhesüsteemid. Varisenud materjal akumuleerub panga jalamile, pakkudes osalist või täielikku kaitset tormilainetuse eest.

Mehitamata õhusõidukeid ja neile paigaldatavaid sensoreid kasutatakse ülemaailmselt ja Euroopa rannikuuuringutes laialdaselt, samas kui Eestis on nende rakendamine olnud seni vähene. Käesolevas uuringus osutus UAV-SfM-fotogrammeetriline modelleerimine väärtuslikuks tööriistaks pankranniku muutuste tuvastamisel ja võimalike georiskide hindamisel. See ületab traditsioonilise 2D-kaardistamise piirangud, pakkudes nii suuremat täpsust kui ka ulatuslikumat ruumilist katvust. See loob aluse detailsele geomorfoloogilisele analüüsile, mis hõlmab nii struktuurigeoloogilist kaardistamist kui ka erosiooni mahu hindamist. Kuigi mudelid võimaldavad hinnata rannikuprotsesside ulatust ja uurida tulevikustsenaariume, on täpsete prognooside koostamine endiselt keeruline, kuna taganemine võib ajas ja ruumis varieeruda ning sõltuda panga geomeetriast. Tervikliku rannikusüsteemi mõistmiseks oleks mudelitesse vaja kaasata ka mereline komponent, kuna Pakri rannikule omane abrasiooniplatvorm ja madalmere üldine batümeetria mõjutavad rannikuprotsesse nii siin kui ka teistes Eesti randades.